

The fundamental plane of black hole activity for low-luminosity radio active galactic nuclei across $0 < z < 4$

Yijun Wang^{1,2} , Tao Wang^{1,2} , Luis C. Ho^{3,4} , Yuxing Zhong⁵, Bin Luo^{1,2}

¹ School of Astronomy and Space Science, Nanjing University, Nanjing 210093, China
e-mail: wangyijun@nju.edu.cn taowang@nju.edu.cn

² Key Laboratory of Modern Astronomy and Astrophysics (Nanjing University), Ministry of Education, Nanjing 210093, China

³ Kavli Institute for Astronomy and Astrophysics, Peking University, Beijing 100871, China

⁴ Department of Astronomy, School of Physics, Peking University, Beijing 100871, China

⁵ Department of Pure and Applied Physics, Waseda University, 3-4-1 Okubo, Shinjuku, Tokyo 169-8555, Japan

February 29, 2024

ABSTRACT

Context. The fundamental plane of black hole activity describes the correlation between radio luminosity (L_R), X-ray luminosity (L_X), and black hole mass (M_{BH}). It reflects a connection between accretion disc and jet. However, the dependence of the fundamental plane on various physical properties of active galactic nuclei (AGNs) and host galaxies remains unclear, especially for low-luminosity AGNs, which is important for understanding the accretion physics in AGNs.

Aims. Here we explore the dependence of the fundamental plane on radio-loudness, Eddington-ratio (λ_{Edd}), redshift, and galaxy star-formation properties (star forming galaxies and quiescent galaxies) across $0.1 < z \leq 4$ for radio AGNs. Based on current deep and large surveys, our studies can extend to lower luminosities and higher redshifts.

Methods. From the deep and large multi-wavelength surveys in the GOODS-N, GOODS-S, and COSMOS/UltraVISTA fields, we constructed a large and homogeneous radio AGN sample consisting of 208 objects with available estimates for L_R and L_X . Then we divided the radio AGN sample into 141 radio-quiet AGNs and 67 radio-loud AGNs according to the radio-loudness defined by the ratio of L_R to L_X , and explored the dependence of the fundamental plane on different physical properties of the two populations, separately.

Results. The ratio of L_R to L_X shows a bimodal distribution which is well described by two single gaussian models. The cross point between these two gaussian components corresponds to a radio-loudness threshold of $\log(L_R/L_X) = -2.73$. The radio-quiet AGNs have significantly larger Eddington ratio than the radio-loud AGNs. Our radio-quiet and radio-loud AGNs show significantly different fundamental plane which is $\log L_R = (0.55 \pm 0.05) \log L_X + (0.28 \pm 0.06) \log M_{BH} + (13.54 \pm 2.27)$ for the radio-quiet AGNs, and $\log L_R = (0.82 \pm 0.08) \log L_X + (0.07 \pm 0.08) \log M_{BH} + (5.24 \pm 3.33)$ for the radio-loud AGNs. For both radio-quiet and radio-loud AGNs, the fundamental plane does not show a significant dependence on redshift and galaxy star-formation properties, while it shows a significant dependence on λ_{Edd} .

Conclusions. The fundamental plane sheds important light on the accretion physics of central engines. Radio-quiet AGNs at $0.01 < \lambda_{Edd} < 0.1$ are consistent with a combination of advection dominated accretion flow (ADAF) and a synchrotron jet model, while at $0.1 < \lambda_{Edd} < 1$, they mainly follow the synchrotron jet model. Radio-loud AGNs are consistent with a combination of ADAF and the synchrotron jet model at $\lambda_{Edd} < 0.01$, and agree with the synchrotron jet model at $0.01 < \lambda_{Edd} < 0.1$, and follow a combination of the standard thin disc and a jet model at $\lambda_{Edd} > 0.1$.

Key words. galaxies: active – galaxies: general – galaxies: nuclei – radio continuum: galaxies – X-rays: galaxies

1. Introduction

Accreting supermassive black holes (SMBHs), also known as active galactic nuclei (AGNs), emit immense energy across the whole electromagnetic spectrum which are believed to have a great impact on the growth and evolution of host galaxies (Fabian 2012; King & Pounds 2015, for reviews). Thus, AGNs are ideal laboratories to explore both accretion physics around black holes and their connection with host galaxies. Accretion physics around black holes are found to be scale-invariant across black hole mass scale from ~ 10 solar masses of X-ray binaries (XRBs) to $10^6 \sim 10^{10}$ solar masses of SMBHs (Merloni et al. 2003; Falcke et al. 2004; Done & Gierliński 2005; McHardy et al. 2006; Kording 2014; Ruan et al. 2019). One of the most prominent pieces of evidences to support the unification of XRBs and SMBHs is the fundamental plane of black

hole activity (Merloni et al. 2003; Falcke et al. 2004, and references therein) that is characterized by a non-linear empirical relation given by radio luminosity, X-ray luminosity and black hole mass. The radio luminosity is thought to be related with jet activities (Begelman et al. 1984), while the ratio of X-ray luminosity to black hole mass is usually taken as a tracer for accretion rate of disc (Haardt & Maraschi 1991; Liu & Qiao 2022). Thus, the fundamental plane connecting XRBs and SMBHs suggests a similar disc-jet connection across different mass scales (e.g., Merloni et al. 2003; Falcke et al. 2004; Plotkin et al. 2012; Dong et al. 2014). The fundamental plane also provides an approach to estimating black hole mass directly through radio luminosity and X-ray luminosity (e.g., Merloni et al. 2003, and references therein).

However, a growing number of studies focusing only on the fundamental plane of AGNs demonstrate that different types

of AGN, such as low-ionization nuclear emission line regions (LINERS), Seyferts, and quasars, show different fundamental planes (e.g., Yuan et al. 2009; Gültekin et al. 2009b; Bonchi et al. 2013; Saikia et al. 2015; Nisbet & Best 2016; Fan & Bai 2016; Xie & Yuan 2017; Li & Gu 2018; Bariuan et al. 2022). These results indicate that the fundamental plane may depend on the accretion state of disc or be sensitive to the adopted sample of black holes (Plotkin et al. 2012). In order to increase sample sizes, the majority of above-mentioned studies about the fundamental plane used a combination of radio-quiet and radio-loud AGNs. For the first time, Wang et al. (2006) and Li et al. (2008) studied the fundamental plane in broad-line radio-quiet and radio-loud AGNs separately. More recently, Bariuan et al. (2022) focused on radio-quiet and radio-loud quasars. These works all found that radio-quiet and radio-loud AGNs show quite different fundamental planes and follow different theoretical accretion models given by Merloni et al. (2003). Due to limitations of data, these works mainly focus on high-luminosity radio-loud and radio-quiet AGNs. Thanks to the deep and large multi-wavelength surveys in the GOODS-N, the GOODS-S, and the COSMOS/ULtraVISTA fields (e.g., Owen 2018; Albers et al. 2020; Smolčić et al. 2017; Liu et al. 2018; Jin et al. 2018), we can extend the fundamental plane studies to low-luminosity radio-quiet and radio-loud AGNs.

Due to the limitation of sample sizes, in the past it is difficult to make detailed analysis for the dependence of the fundamental plane on other physical properties, such as 1) Eddington ratio, 2) redshift, and 3) galaxy star-formation properties, especially for low-luminosity AGNs. These studies may be crucial to our understanding of why different types of AGNs exhibit different fundamental planes. 1) “Eddington ratio”: Observational evidences show that radio-quiet and radio-loud AGNs have different fundamental planes (Wang et al. 2006; Li et al. 2008; Bariuan et al. 2022), and radio-loudness exhibits a negative correlation with Eddington ratio (Ho 2002; Panessa et al. 2007; Sikora et al. 2007). This demonstrates that the fundamental plane may depend on Eddington-scaled accretion rate, which is still lack of quantitative studies until now. 2) “Redshift”: AGN accretion rate density peaks at $z \sim 2$, and declines toward local universe (see Aird et al. 2010; Madau & Dickinson 2014, for a review), which may give rise to different accretion physics at different cosmic time. The majority of previous works studied the fundamental plane at low redshift ($z < 0.5$), while some of them extended to high redshift but only for high-luminosity AGNs (Wang et al. 2006; Li et al. 2008; Bariuan et al. 2022). For low-luminosity AGNs, it is still unclear about the dependence of the fundamental plane on redshift. 3) “Galaxy star-formation properties”: Radio AGNs hosted by star forming galaxies (SFGs) and quiescent galaxies (QGs) have different cosmic evolutions for AGN incident rate (e.g., Janssen et al. 2012; Kondapally et al. 2022; Wang et al. 2024, hereafter “Paper I”) and radio luminosity functions (Kondapally et al. 2022, Paper I). Given that SFGs and QGs may perform different fueling mechanisms toward central SMBHs (e.g., Kauffmann & Heckman 2009; Kondapally et al. 2022; Ni et al. 2023), radio activities of central engines may depend on the fueling mechanisms of their host galaxies. Further, it still remains unclear that whether the fueling mechanisms affect the disc-jet connection characterized by the fundamental plane.

In this work, we first introduce a parent radio AGN sample from the GOODS-N, the GOODS-S, and the COSMOS/ULtraVISTA fields selected by Paper I across $0.1 < z \leq 4$ (Section 2). For these radio AGNs, we collect available measurements for radio luminosity and X-ray luminosity from our previous works and other literature works, and infer black hole mass from stel-

lar mass (Section 3). Next we divide our sample into radio-quiet and radio-loud AGN subsamples according to the radio loudness defined by the relative strength of the radio and X-ray emission (Section 4). Then we fit the fundamental plane for the radio-quiet and radio-loud AGN subsamples separately (Section 5). Further, we give a brief summary about the fundamental plane studies and discuss the dependence of the fundamental plane on Eddington ratio, redshift, and galaxy star-formation properties (Section 6). In Section 6, we also discuss the central engines for radio-quiet and radio-loud AGNs. Finally, we summarize our conclusions in Section 7. Throughout this paper, we assume a Chabrier (2003) initial mass function (IMF) and a flat cosmology with the following parameters: $\Omega_m = 0.3$, $\Omega_\Lambda = 0.7$, and $H_0 = 70 \text{ km s}^{-1} \text{ Mpc}^{-1}$.

2. Parent radio AGN sample

2.1. GOODS-N and COSMOS fields

For the GOODS-N and the COSMOS/ULtraVISTA fields, our parent radio AGN sample was derived from Paper I, which consists of 102 radio AGNs from the GOODS-N and 881 radio AGNs from the COSMOS/ULtraVISTA across $0.1 < z < 4$ selected by the infrared-radio correlation (IRRC; e.g., Helou et al. 1985; Condon 1992, and references therein). We refer to Section 4 in Paper I for more details about sample selections and here we just give a brief introduction. IR emission and radio emission of the star formation process have a mutual origin from activities of massive stars (Condon 1992; Dubner & Giacani 2015), which results in a tight correlation between each other (IRRC). The IRRC is usually defined by the ratio (q_{TIR}) of rest-frame 8–1000 μm IR luminosity (L_{TIR}) to rest-frame 1.4 GHz radio luminosity ($L_{1.4\text{GHz}}$) which is in a form of $q_{\text{TIR}} = \log[L_{\text{TIR}}/(L_{1.4\text{GHz}} \times 3.75 \times 10^{12} \text{ Hz})]$ (Helou et al. 1985). AGNs may have extra radio emission from nuclear activities, such as jets (Panessa et al. 2019, for a review). Therefore, radio AGNs usually exhibit a radio excess relative to the IRRC and have a smaller q_{TIR} value compared to that of star formation. In Paper I, we define a q_{TIR} threshold ($q_{\text{TIR,AGN}}$) to select radio AGNs (see details in Paper I). A radio source will be selected as a radio AGN if its q_{TIR} value is lower than $q_{\text{TIR,AGN}}$. In addition, $L_{1.4\text{GHz}}$ was derived from Paper I which is calculated by the radio flux from the deep VLA 1.4 GHz (GOODS-N; Owen 2018) or 3 GHz radio surveys (COSMOS; Smolčić et al. 2017) assuming a radio spectral index of -0.8 (e.g., Yang et al. 2022). L_{TIR} was derived from Paper I which is estimated by the broadband spectral energy distribution (SED) fitting. In the SED fitting process, the far-infrared (FIR) and submillimeter data are derived from the “super de-blended” photometry (Liu et al. 2018; Jin et al. 2018) ensuring a more precise estimate for the IR luminosity.

2.2. GOODS-S field

We also selected a radio AGN sample from the GOODS-S field following Paper I to enlarge our sample. We first derived radio data at 3 GHz from Albers et al. (2020) which contains 712 sources with signal-to-noise ratio (S/N) larger than 3. Then we cross-matched this 3 GHz catalog with the ultraviolet-optical-mid-infrared (UV-optical-MIR) catalog from Guo et al. (2013) by a match radius of 1 arcsec. This UV-optical-MIR catalog covers the wavelength range between 0.4 and 8 μm , and contains 34,930 sources over 171 arcmin². After cross-matching, 414 (out of 712) radio objects in Albers et al. (2020) have UV/optical/MIR counterparts in Guo et al. (2013). Following

selection criteria in Paper I ($0.1 < z \leq 4.0$ and S/N of radio flux ≥ 5), we selected out 366 radio sources from the 414 objects as our radio sources sample in the GOODS-S field to make further analysis. Next we collected MIR-FIR data in the GOODS-S field from Wang et al. (in prep.). Based on the similar “super de-blended” photometry method in the GOODS-N and COSMOS fields, Wang et al. (in prep.) obtained photometry at MIR band (*Spitzer* 16 and 24 μm) and “super de-blended” photometry at FIR band (*Herschel* 100, 160, 250, 350, and 500 μm) for 1881 objects. We also utilized the submillimeter data derived from SCUBA-2 850 μm survey (Cowie et al. 2018), Atacama Large Millimeter/submillimeter Array (ALMA) 870 μm survey (Tadaki et al. 2020), and ALMA 1.1 mm survey (Gómez-Guijarro et al. 2022). Further, we cross-matched the radio sources sample in the GOODS-S field with the MIR-FIR catalog (Wang et al. in prep.) by a match radius of 1 arcsec, with the SCUBA-2 850 μm survey by a radius of 5 arcsec, with the ALMA 870 μm survey by a radius of 1 arcsec, with the ALMA 1.1 mm survey by a radius of 1.5 arcsec. For the 366 sources in the radio sources sample, 324 objects have MIR-FIR counterparts in Wang et al. (in prep.). Of these, 27 (out of 324) objects have SCUBA-2 850 μm detections, 12 (out of 324) objects have ALMA 870 μm detections, and 35 (out of 324) objects have ALMA 1.1 mm detections. For the above-mentioned 324 objects that have multi-wavelength data from UV-optical-MIR to FIR-submillimeter-radio bands, we performed broadband SED fitting with Code Investigating GALaxy Emission (CIGALE 2022.0; Burgarella et al. 2005; Noll et al. 2009; Boquien et al. 2019; Yang et al. 2020, 2022) to estimate various galaxy properties (such as L_{TIR} and stellar mass M_\star). We refer to Appendix A in Paper I for parameter settings about the SED fitting. Finally, we followed Paper I to select a parent radio AGN sample in the GOODS-S field including 71 sources across $0.1 < z \leq 4.0$ (see brief introduction in Section 2.1 and detailed analysis in Section 4 of Paper I).

3. Derived quantities

3.1. Black hole mass (M_{BH})

In this work we estimated black hole mass through an indirect way that is based on the correlation between black hole mass and total stellar mass ($M_{\text{BH}}-M_\star$ relation; e.g., Greene et al. 2020, for a review). Here M_\star was estimated by the broadband SED fitting (see details in Paper I for the GOODS-N and COSMOS fields, and see details in Section 2.2 for the GOODS-S field). Most of our radio AGN sample are hosted by ellipticals. Thus, we used the $M_{\text{BH}}-M_\star$ relation in a form of $\log(M_{\text{BH}}/M_\odot) = (7.89 \pm 0.09) + (1.33 \pm 0.12) \times \log(M_\star/3 \times 10^{10} M_\odot)$ from Greene et al. (2020) for local early-type galaxies. The M_\star in this work was estimated based on a Chabrier (2003) IMF, while Greene et al. (2020) adopted a diet Salpeter IMF (Bell et al. 2003). Thus, we divided our M_\star by a constant value of 1.14 (Madau & Dickinson 2014; van der Wel et al. 2007) to convert values from the Chabrier (2003) IMF to the diet Salpeter IMF. In addition, Li et al. (2023) found that the $M_\star-M_{\text{BH}}$ relation does not show a significant evolution with redshift across $0 < z < 3.5$. Therefore, we applied the local $M_\star-M_{\text{BH}}$ relation from Greene et al. (2020) to the whole redshift range in this work ($0.1 < z < 4$). The uncertainties of M_{BH} were inferred from the parameters errors of $M_{\text{BH}}-M_\star$ relation (Greene et al. 2020) using the propagation of error method.

3.2. Rest-frame 5 GHz radio luminosity (L_{R})

To get a pure radio luminosity for AGNs, radio luminosity from star formation (L_{SF}) should be subtracted from the total radio luminosity. The L_{SF} can be estimated by the IRRC in the form of

$$L_{1.4\text{GHz,SF}} = L_{\text{TIR}} / (3.75 \times 10^{12} \text{ Hz} \times 10^{q_{\text{TIR}}}) \quad (1)$$

(Helou et al. 1985), where L_{TIR} is the rest-frame 8–1000 μm IR luminosity, $L_{1.4\text{GHz,SF}}$ is the rest-frame 1.4 GHz radio luminosity from star formation in the unit of $\text{erg s}^{-1} \text{ Hz}^{-1}$, and q_{TIR} is the IRRC index for the star-formation. The q_{TIR} is found to depend on redshift (Magnelli et al. 2015; Delhaize et al. 2017; Novak et al. 2017; Enia et al. 2022) and stellar mass (Delvecchio et al. 2022). For consistency, here we used the relation obtained in our Paper I which is in a form of $q_{\text{TIR}} = (2.62 \pm 0.08) \times (1+z)^{-0.08 \pm 0.03}$. In Paper I, we did not consider a M_\star -dependent IRRC as it does not have a significant impact on our results.

Then the rest-frame 5 GHz radio luminosity from AGN (hereafter L_{R} ; in the unit of erg s^{-1}) is calculated by

$$L_{\text{R}} = \frac{4\pi D_L^2}{(1+z)^{1+\alpha_{\text{AGN}}}} \times \left(\frac{5 \text{ GHz}}{\nu_{\text{obs}}} \right)^{\alpha_{\text{AGN}}} \times (S_{\nu_{\text{obs}}} - S_{\nu_{\text{SF}}}) \times 5 \text{ GHz}, \quad (2)$$

where D_L is the luminosity distance (in the unit of centimeter), z is the redshift, α_{AGN} is the radio spectral index for AGNs that is assumed to be -0.5 (e.g., de Gasperin et al. 2018; Bariuan et al. 2022), ν_{obs} is the observed frequency (in the unit of GHz), and $S_{\nu_{\text{obs}}}$ (in the unit of $\text{erg s}^{-1} \text{ cm}^{-2} \text{ Hz}^{-1}$) is the observed integrated flux densities at ν_{obs} . For the GOODS-N, $S_{\nu_{\text{obs}}}$ at $\nu_{\text{obs}} = 1.4$ GHz was derived from Owen (2018) (see Section 2.1 or Paper I). For the GOODS-S, $S_{\nu_{\text{obs}}}$ at $\nu_{\text{obs}} = 3$ GHz was derived from Alberts et al. (2020) (see Section 2.2). For the COSMOS, $S_{\nu_{\text{obs}}}$ at $\nu_{\text{obs}} = 3$ GHz was derived from Smolčić et al. (2017) (see Section 2.1 or Paper I). Here $S_{\nu_{\text{SF}}}$ is the flux densities at ν_{obs} attributed to the star formation, which is calculated by

$$S_{\nu_{\text{SF}}} = L_{1.4\text{GHz,SF}} \frac{(1+z)^{1+\alpha_{\text{SF}}}}{4\pi D_L^2} \left(\frac{\nu_{\text{obs}}}{1.4 \text{ GHz}} \right)^{\alpha_{\text{SF}}} \quad (3)$$

(Condon 1992), where $L_{1.4\text{GHz,SF}}$ is given by Equation 1 and α_{SF} is the radio spectral index for star formation that is assumed to be -0.8 (e.g., Yang et al. 2022). The uncertainties of L_{R} were inferred from the flux uncertainties given by the above-mentioned radio surveys using the propagation of error method.

In some literature works, the rest-frame 5 GHz radio luminosity in the fundamental plane refers to the nuclear radio emission from a compact radio core in order to compare with X-ray emission that are mainly from central engine. However, VLA 1.4 GHz or 3 GHz surveys in the GOODS-N, the GOODS-S, and the COSMOS fields do not have high enough spatial resolution to resolve the compact radio core. Even so, their spatial resolutions still ensure that the radio flux is measured on the top of the galaxy rather than the large-scale jet. In addition, nearly 20% of our sample have radio detections with higher spatial resolution, such as VLA 10 GHz Pilot Survey in the GOODS-N field (average spatial resolution of $0.22'' \approx 1.76 \text{ kpc}$ at $z = 1$; Murphy et al. 2017) and VLA 6 GHz Survey in the GOODS-S field (average angular resolution of $0.62'' \times 0.31'' \approx 4.97 \text{ kpc} \times 2.48 \text{ kpc}$ at $z = 1$; Alberts et al. 2020; Lyu et al. 2022). These objects do not show significant large-scale jet structures. Furthermore, we utilized the ratio of peak radio flux to total radio flux as a proxy for compactness to select out a sample only including objects with relatively compact structure (including 110 sources). We found

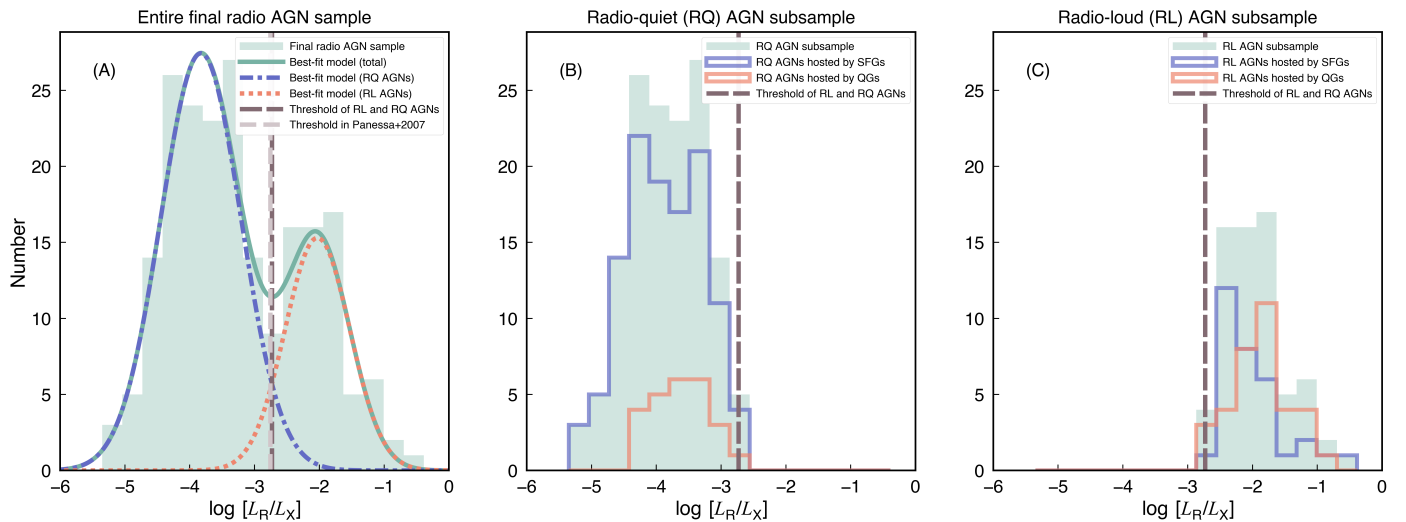


Fig. 1: Distribution of the ratio of the rest-frame 5 GHz radio luminosity (L_R) to the rest-frame 2–10 keV X-ray luminosity (L_X) for the entire final radio AGNs sample (Panel A), the radio-quiet (RQ) AGN subsample (Panel B), and the radio-loud (RL) AGN subsample (Panel C). The green solid curve in Panel (A) represents the best-fit model to the entire distribution, which consists of two single Gaussian models (the blue dash-dotted curve and the red dotted curve). The vertical dark-gray dashed line in all panels represents the cross point between two single models, which is defined as the radio-loudness threshold to divide radio-loud and radio-quiet AGNs in this work. The vertical light-gray dashed line in Panel (A) represents the radio-loudness threshold in [Panessa et al. \(2007\)](#), which is obtained by a sample consisting of local Seyferts and low luminosity radio galaxies (LLRGs). The blue and red histograms in Panel (B) represent the radio-quiet AGNs hosted by SFGs and QGs, respectively, while in Panel (C), they represent the radio-loud AGNs hosted by SFGs and QGs, respectively.

that using this compact objects subsample does not change our results comparing to using the entire sample. In order to ensure a large sample to make analysis, in this work we used the entire sample and do not consider whether the rest-frame 5 GHz radio luminosity is strictly derived from a spatially-resolved compact core.

3.3. Rest-frame 2–10 keV X-ray luminosity (L_X)

X-ray data in the GOODS-N were mainly derived from the 2 Ms *Chandra* Deep Field-North (CDF-N) survey ([Xue et al. 2016](#)). [Xue et al. \(2016\)](#) estimated the absorption-corrected rest-frame 0.5–7 keV luminosity assuming an intrinsic photon index of $\Gamma = 1.8$ (typical value for the X-ray spectrum of AGNs; [Tozzi et al. 2006](#)). Then we cross-matched our parent radio AGN sample in the GOODS-N (102 objects, see Section 2.1) with the 2 Ms CDF-N survey by a match radius of 1.5 arcsec. A total of 46 (out of 102) objects have X-ray counterparts and their intrinsic 2–10 keV luminosities used in this work are calculated by the intrinsic 0.5–7 keV luminosity from [Xue et al. \(2016\)](#) under the assumption of $\Gamma = 1.8$. Among these 46 objects, 17 sources have been performed with systematic X-ray spectral analysis in [Li et al. \(2019\)](#) (Γ is a free parameter in the fit and $\Gamma = 1.80 \pm 0.08$ for these objects). Therefore, for these 17 sources, their intrinsic 2–10 keV luminosities were derived from [Li et al. \(2019\)](#).

X-ray data in the GOODS-S were mainly derived from the 7 Ms *Chandra* Deep Field-South (CDF-S) survey ([Luo et al. 2017](#)). Similar to the GOODS-N, the absorption-corrected rest-frame 0.5–7 keV luminosities in the GOODS-S are estimated by assuming an intrinsic photon index of $\Gamma = 1.8$ ([Luo et al. 2017](#)). We cross-matched our parent radio AGN sample in the GOODS-S (71 objects, see Section 2.2) with the 7 Ms CDF-S survey by a match radius of 1.5 arcsec. A total of 48 (out of 71) objects have X-ray counterparts and their intrinsic 2–10 keV luminosities

used in this work are calculated by the intrinsic 0.5–7 keV luminosity from [Luo et al. \(2017\)](#) under the assumption of $\Gamma = 1.8$. Among these 48 objects, 23 sources have been performed with systematic X-ray spectral analysis in [Liu et al. \(2017\)](#) (Γ is a free in the fit and $\Gamma = 1.81 \pm 0.09$). Therefore, for these 23 sources, their intrinsic 2–10 keV luminosities were derived from [Liu et al. \(2017\)](#).

X-ray data in the COSMOS were mainly derived from the X-ray spectral fitting for the 4.6 Ms *Chandra* COSMOS-Legacy survey ([Marchesi et al. 2016](#)) that gives the intrinsic 2–10 keV luminosity. We cross-matched our parent radio AGN sample in the COSMOS/UltraVISTA (881 objects, see Section 2.1) with the 4.6 Ms *Chandra* COSMOS-Legacy survey by a match radius of 1.5 arcsec. A total of 117 (out of 881) objects have X-ray counterparts with available estimates for the intrinsic 2–10 keV luminosity ($\Gamma = 1.85 \pm 0.62$). Among these 117 objects, 8 objects are classified as Compton-thick AGN by [Lanzuisi et al. \(2018\)](#). For these 8 objects, we used their obscuration-corrected intrinsic 2–10 keV luminosity from [Lanzuisi et al. \(2018\)](#) to make the subsequent analysis.

The above-mentioned 2–10 keV luminosity refers to the total X-ray luminosity from the entire galaxy ($L_{2-10\text{keV,tot}}$). In order to get the pure X-ray luminosity from AGNs, X-ray radiation from XRBs should be subtracted. X-ray luminosities of XRBs have been found to correlate with star formation rate (SFR) and stellar mass ([Grimm et al. 2003](#); [Lehmer et al. 2010](#); [Mineo et al. 2012, 2014](#)), which also shows an evolution with redshift ([Lehmer et al. 2016](#)). Here we used the relation of

$$\frac{L_{2-10\text{keV,XRBs}}}{\text{erg s}^{-1}} = 10^{29.3} (1+z)^{2.19} \frac{M_{\star}}{M_{\odot}} + 10^{39.4} (1+z)^{1.02} \frac{\text{SFR}}{M_{\odot} \text{ yr}^{-1}} \quad (4)$$

derived from [Lehmer et al. \(2016\)](#) based on the 6Ms CDF-S survey. The M_{\star} and SFR in this relation were estimated assuming a [Kroupa \(2001\)](#) IMF while we used the [Chabrier \(2003\)](#) IMF

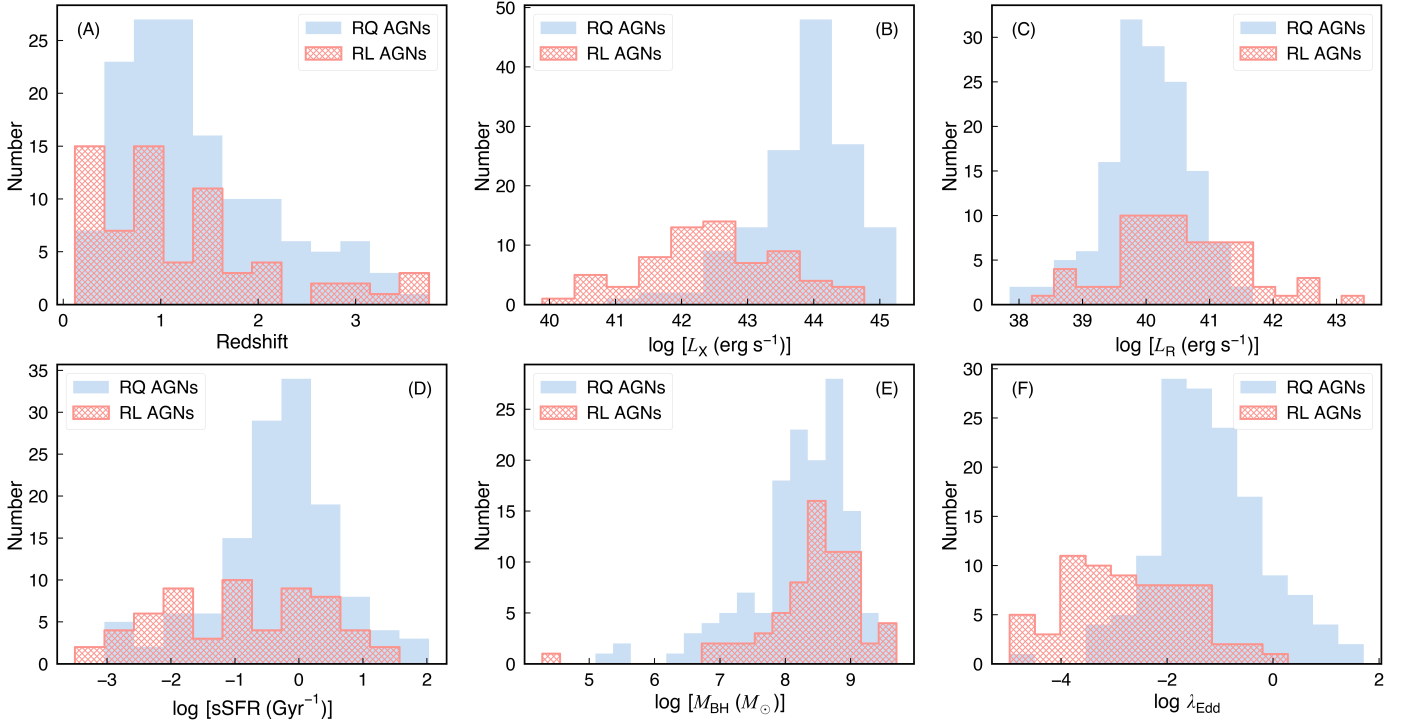


Fig. 2: Distribution of physical properties for the radio-quiet (RQ) AGNs (blue histogram) and radio-loud (RL) AGNs (red histogram) used to study the fundamental plane of black hole activity, including: (A) redshift, (B) rest-frame 2–10 keV X-ray luminosity from AGNs (L_X), (C) rest-frame 5 GHz radio luminosity from AGNs (L_R), (D) specific star formation rate (sSFR), (E) black hole mass (M_{BH}) inferred from stellar mass, (F) Eddington ratio (λ_{Edd}).

throughout this work. Therefore, we first divided our M_\star and SFR by a constant factor of 1.06 (Speagle et al. 2014) to convert values from the Chabrier (2003) IMF to the Kroupa (2001) IMF. Then we applied the scaled M_\star and SFR into Equation 4 to get the X-ray luminosity from XRBs. Finally, the pure X-ray luminosity from AGNs (hereafter L_X ; in the unit of erg s^{-1}) can be calculated by

$$L_X = L_{2-10\text{keV,tot}} - L_{2-10\text{keV,XRBs}}, \quad (5)$$

where $L_{2-10\text{keV,XRBs}}$ is calculated by Equation 4. The uncertainties of L_X were inferred from the flux uncertainties given by the above-mentioned X-rays surveys using the propagation of error method.

Considering the available estimates for M_\star , L_R and L_X (L_X in Equation 5 is required to be greater than 0), we selected out a radio AGNs sample including 208 objects (46 objects in the GOODS-N, 45 objects in the GOODS-S, and 117 objects in the COSMOS/UltraVISTA) that are utilized in the subsequent analysis for the fundamental plane. The basic information for these 208 objects are summarized in Table A1. In addition, for the radio AGNs without X-ray counterparts in the aforementioned X-ray surveys, we estimated their 2–10 keV X-ray luminosity upper limits by the X-ray detection limit in these three fields (Xue et al. 2016; Luo et al. 2017; Civano et al. 2016) assuming $\Gamma = 1.8$. The X-ray detection limit is $2.0 \times 10^{-16} \text{ erg cm}^{-2} \text{ s}^{-1}$ in the 0.5–7 keV band for the GOODS-N (Xue et al. 2016), $1.9 \times 10^{-17} \text{ erg cm}^{-2} \text{ s}^{-1}$ in the 0.5–7 keV band for the GOODS-S (Luo et al. 2017), and $1.5 \times 10^{-15} \text{ erg cm}^{-2} \text{ s}^{-1}$ in the 2–10 keV band for the COSMOS (Civano et al. 2016).

4. Final sample of Radio-loud and Radio-quiet AGNs

In this work, our final radio AGN sample used to make the fundamental plane analysis consists of the above-mentioned 208 objects which have available estimates for L_R , L_X , and inferred M_{BH} from M_\star . Then we utilized the radio-loudness defined by the relative strength of the radio and X-ray emission (R_X ; e.g., Terashima & Wilson 2003; Panessa et al. 2007; Ho 2008) to divide radio-loud and radio-quiet AGNs in this work. The ratio of L_R to L_X is shown in Panel (A) of Fig. 1. The $\log(L_R/L_X)$ distribution shows a bimodal shape which is attributed to radio-quiet and radio-loud AGNs, respectively. Then we used two single Gaussian components to model the double peaks (see the blue dash-dotted line and red dotted line in Panel A of Fig. 1), and used their cross point as the radio-loudness threshold (see the vertical dark-gray dashed line in Panel A of Fig. 1) to divide radio-quiet and radio-loud AGNs in this work. This radio-loudness threshold ($R_{X,T}$) is

$$R_{X,T} = \log(L_R/L_X)_{\text{cross point}} = -2.73. \quad (6)$$

It is consistent with the result in Panessa et al. (2007) that is obtained based on a sample of 47 local Seyferts and 16 local low-luminosity radio galaxies (see the vertical light-gray dashed line in Panel A of Fig. 1). Finally, we selected out 141 radio-quiet AGNs (68% of the final radio AGN sample) and 67 radio-loud AGNs (32% of the final radio AGN sample). The physical properties of these radio-quiet and radio-loud AGNs are shown in Fig. 2.

- (1) Both the radio-loud and radio-quiet AGN subsamples have a similar redshift range between 0.1 and 4, while the median

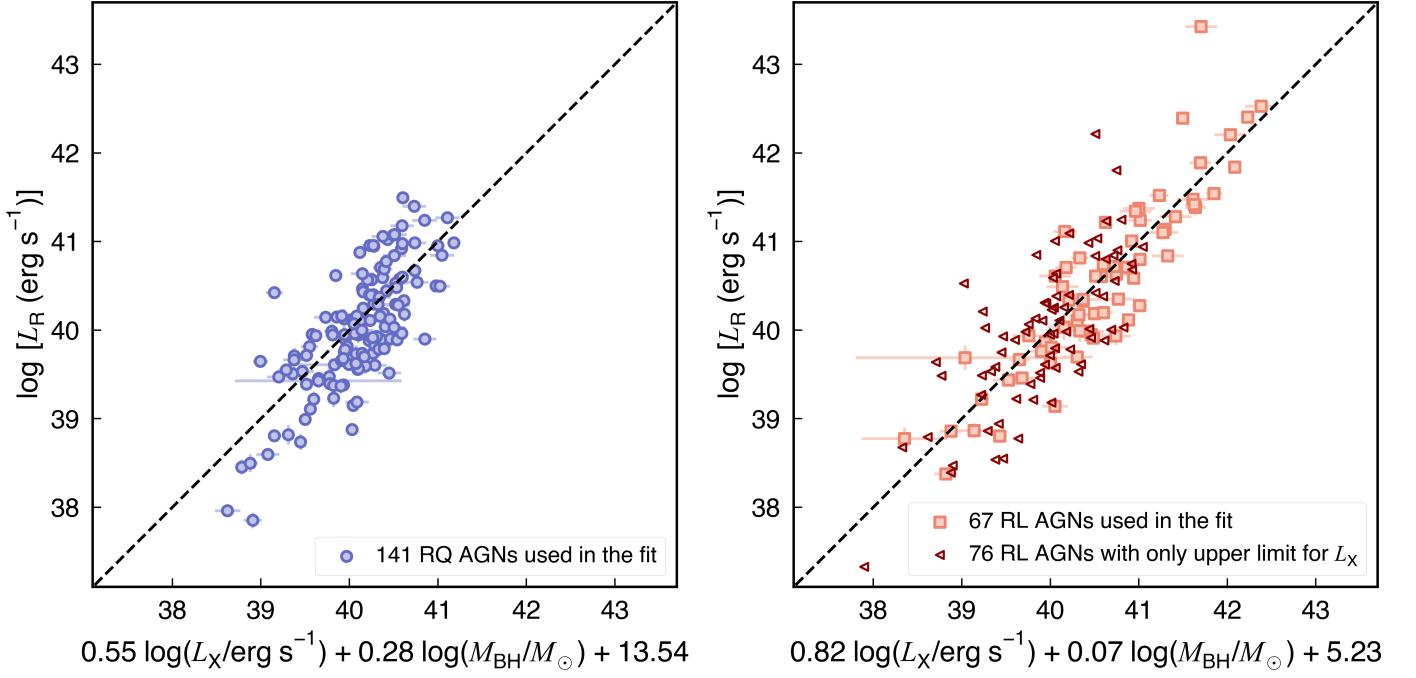


Fig. 3: Comparison of the predicted rest-frame 5 GHz luminosity from the best-fit fundamental plane (x axis) and the observed rest-frame 5 GHz luminosity (y axis) for the radio-quiet AGNs (left panel) and the radio-loud AGNs (right panel). The black dashed line in each panel represents the 1:1 line. The dark-red empty triangles in the right panel represent the radio-loud AGNs with only upper limits for L_X (see parameter calculation in Section 3.3 and see sample selection in Section 5).

redshift is 0.9 for the radio-loud AGNs and 1.2 for the radio-quiet AGNs (see Panel A of Fig. 2).

- (2) The range of $\log[L_X \text{ (erg s}^{-1}\text{)]}$ for our radio-quiet AGN sample is between 40.9 and 45.2 with a median of 44.0, while for our radio-loud AGN sample, it is between 39.9 and 44.7 with a median of 42.4 (see Panel B of Fig. 2). The radio-quiet AGN sample has significantly larger L_X than the radio-loud AGN sample.
- (3) The range of $\log[L_R \text{ (erg s}^{-1}\text{)]}$ for the radio-quiet AGN sample is between 37.9 and 41.5 with a median of 40.0, while for the radio-loud AGN sample, it is between 38.4 and 43.4 with a median of 40.5 (see Panel C of Fig. 2). The radio-quiet AGN sample has slightly lower L_R than the radio-loud AGN sample.
- (4) The range of specific star formation rate (sSFR) for our radio-quiet AGN sample is between 0.001 and 100 Gyr^{-1} with a median of 0.60 Gyr^{-1} , while for our radio-loud AGN sample, it is between 0.003 and 17 Gyr^{-1} with a median of 0.12 Gyr^{-1} (see Panel D of Fig. 2). Here SFR was derived from Paper I which is estimated by the broadband SED fitting. The radio-quiet AGN sample has slightly higher sSFR than the radio-loud AGN sample.
- (5) The range of $\log[M_{\text{BH}}/M_\odot]$ for the radio-quiet AGN sample is between 5.35 and 9.62 with a median of 8.36, while for the radio-loud AGN sample, it is between 4.28 and 9.70 with a median of 8.58 (see Panel E of Fig. 2). The radio-quiet AGN sample has slightly lower M_{BH} than the radio-loud AGN sample.
- (6) The Eddington ratio (λ_{Edd}) is defined as $\lambda_{\text{Edd}} = L_{\text{bol}}/L_{\text{Edd}}$ where L_{bol} is the bolometric luminosity and L_{Edd} is the Eddington luminosity. The bolometric luminosity is converted from X-ray luminosity by a bolometric correction factor that is related to the luminosity (e.g., Duras et al. 2020). For our sample, this correction factor is around 20

(Duras et al. 2020). Therefore, here L_{bol} is calculated by $L_{\text{bol}} = L_X \times 20$. The Eddington luminosity is defined as $L_{\text{Edd}} = 1.3 \times 10^{38} M_{\text{BH}}/M_\odot$ in the unit of erg s^{-1} (Rybicki & Lightman 1979). The range of λ_{Edd} for our radio-quiet AGN sample is between 2.3×10^{-5} and 51 with a median of 0.06, while for our radio-loud AGN sample, it is between 10^{-5} and 1.0 with a median of 0.001 (see Panel F of Fig. 2). The radio-quiet AGN sample has significantly larger λ_{Edd} than the radio-loud AGN sample, which is consistent with the negative correlation between radio-loudness and Eddington ratio (e.g., Ho 2002; Panessa et al. 2007; Sikora et al. 2007).

5. Fitting the fundamental plane for radio-loud and radio-quiet AGNs

Following Merloni et al. (2003), we defined the fundamental plane of black hole activity as

$$\log L_R = \xi_X \log L_X + \xi_M \log M_{\text{BH}} + b, \quad (7)$$

where L_R is the rest-frame 5 GHz radio luminosity (in the unit of erg s^{-1}), L_X is the rest-frame 2–10 keV X-ray luminosity (in the unit of erg s^{-1}), M_{BH} is the black hole mass (in the unit of M_\odot). Then we use the ordinary least squares (OLS) Linear Regression method in the Python package SCIKIT-LEARN (Pedregosa et al. 2011) to fit the data set. Further, we ran the fitting process with 4000 iterations to take the uncertainties of both dependent and independent variables into account. Next we take the variable L_X as an example to show the detailed analysis process. In our sample, the i th object has the observed $L_{X,\text{obs},i}$ with an uncertainty of σ_i . In the j th fitting process, value of the variable used for fitting ($L_{X,\text{fit},i,j}$) was randomly selected from a normal distribution centered at $L_{X,\text{obs},i}$ with a variance of σ_i . We made the same value

Table 1: Best-fitting parameters of the fundamental plane of black hole activity for radio-quiet and radio-loud AGNs in this work.

	N_{sources}	ξ_X	ξ_M	b	σ_R
Radio-quiet AGNs					
Total	141	0.55 ± 0.05	0.28 ± 0.06	13.54 ± 2.27	0.37
$\lambda_{\text{Edd}} \leq 10^{-1.5}$	63	0.63 ± 0.09	0.33 ± 0.15	9.76 ± 3.42	0.31
$\lambda_{\text{Edd}} > 10^{-1.5}$	78	0.52 ± 0.13	0.26 ± 0.08	14.99 ± 5.54	0.40
$0.1 < z \leq 1.0$	56	0.53 ± 0.07	0.27 ± 0.08	14.43 ± 3.36	0.35
$1.0 < z \leq 4.0$	85	0.36 ± 0.09	0.30 ± 0.07	21.79 ± 3.83	0.37
Hosted by SFGs	116	0.45 ± 0.07	0.32 ± 0.07	17.63 ± 3.14	0.39
Hosted by QGs	25	0.67 ± 0.06	0.18 ± 0.08	9.23 ± 2.89	0.22
Radio-loud AGNs					
Total	67	0.82 ± 0.08	0.07 ± 0.08	5.24 ± 3.33	0.34
$\lambda_{\text{Edd}} \leq 10^{-2.5}$	40	0.57 ± 0.14	0.24 ± 0.18	14.07 ± 5.43	0.33
$\lambda_{\text{Edd}} > 10^{-2.5}$	27	0.90 ± 0.19	0.07 ± 0.17	1.77 ± 7.39	0.35
$0.1 < z \leq 1.0$	37	0.83 ± 0.09	0.03 ± 0.09	4.98 ± 3.82	0.31
$1.0 < z \leq 4.0$	30	0.81 ± 0.16	0.20 ± 0.19	4.61 ± 7.00	0.37
Hosted by SFGs	32	0.78 ± 0.13	0.13 ± 0.12	6.15 ± 5.30	0.36
Hosted by QGs	35	0.85 ± 0.09	-0.08 ± 0.16	5.17 ± 4.05	0.32

Notes. N_{sources} represents the number of sources. The best-fit parameters for the fundamental plane correspond to the correlation coefficient of X-ray luminosity ξ_X , the correlation coefficient of black hole mass ξ_M , and constant offset b (see Equation 7). Parameter σ_R denotes the scatter of the observed L_R relative to the predicted value from the best-fit fundamental plane.

selection for the variables L_R and M_{BH} . Thus, in the j th fitting process, the i th object had $L_{X,\text{fit},i,j}$, $L_{R,\text{fit},i,j}$, and $M_{\text{BH},\text{fit},i,j}$. After the j th fitting, the best-fit parameters were given as $\xi_{X,j} \pm \sigma_{X,j}$, $\xi_{M,j} \pm \sigma_{M,j}$, and $b_j \pm \sigma_{b,j}$. Finally, fitting with 4000 iterations produced a nearly symmetric distribution for each fitting coefficient. Then we used the mean of the distribution as the best-fit coefficient, while the error was derived from the integrated variance from both fitting process and observed uncertainties. Next we take parameter ξ_X as an example. The best-fit ξ_X was calculated by $\sum_{j=1}^{4000} \xi_{X,j} / 4000$ (written as $\bar{\xi}_X$ hereafter), while its error was calculated by $\sqrt{\sum_{j=1}^{4000} (\xi_{X,j} - \bar{\xi}_X)^2 / 4000 + (\sum_{j=1}^{4000} \sigma_{X,j} / 4000)^2}$. Then we did the same calculation for both ξ_M and b .

We performed the above fitting process for our radio-quiet and radio-loud AGN samples separately. We found a best-fit fundamental plane of

$$\log L_R = (0.55 \pm 0.05) \log L_X + (0.28 \pm 0.06) \log M_{\text{BH}} + (13.54 \pm 2.27) \quad (8)$$

for the radio-quiet AGN sample, and

$$\log L_R = (0.82 \pm 0.08) \log L_X + (0.07 \pm 0.08) \log M_{\text{BH}} + (5.24 \pm 3.33) \quad (9)$$

for the radio-loud AGN sample. The best-fit coefficients and their errors are summarized in Table 1. The comparison between the observed L_R and the predicted L_R by the best-fit fundamental plane is shown in Fig. 3. The significantly different fundamental plane between radio-quiet and radio-loud AGNs, and their

comparison with literature works are discussed in details in Section 6.1. For the radio AGNs with only upper limits for X-ray luminosity, we estimated their radio-loudness lower limits according to the ratio of L_R to L_X -upper-limits. Therefore, from these sources, we selected out 76 radio-loud AGNs with only upper limits for X-ray luminosity (see the dark-red triangles in Fig. 3) based on the previously defined radio-loudness threshold (see Equation 6). These radio-loud AGNs are greatly consistent with the fundamental plane (see Equation 9) obtained with the aforementioned radio-loud AGN sample (see Fig. 3).

6. Discussion

The comparison between the best-fit correlation coefficients ξ_X and ξ_M of the fundamental plane can characterize the accretion physics of central engines (Merloni et al. 2003). In the ξ_X - ξ_M diagram (see Fig. 4, Fig. 5, and Fig. 6), the theoretically predicted correlation coefficients are derived from Merloni et al. (2003) with the electron spectral index $p = 2$. These theoretical models are advection dominated accretion flow (ADAF; a radiatively inefficient accretion flow; Narayan & Yi 1994; Yuan 2001; Yuan & Narayan 2014, for a review), the synchrotron jet model producing radio emission by the optically thin synchrotron radiation from jet, and the standard Shakura-Sunyaev disc model (Shakura & Sunyaev 1973; Pringle 1981, for a review). Next we give a brief summary about the studies for the fundamental plane in Section 6.1 and further discuss the dependence of the fundamental plane on Eddington ratio (Section 6.2), redshift (Section 6.3), and galaxy star-formation properties (Section 6.4). Combining our and literature works, we investigate the central engines of radio-quiet and radio-loud AGNs in Section 6.5.

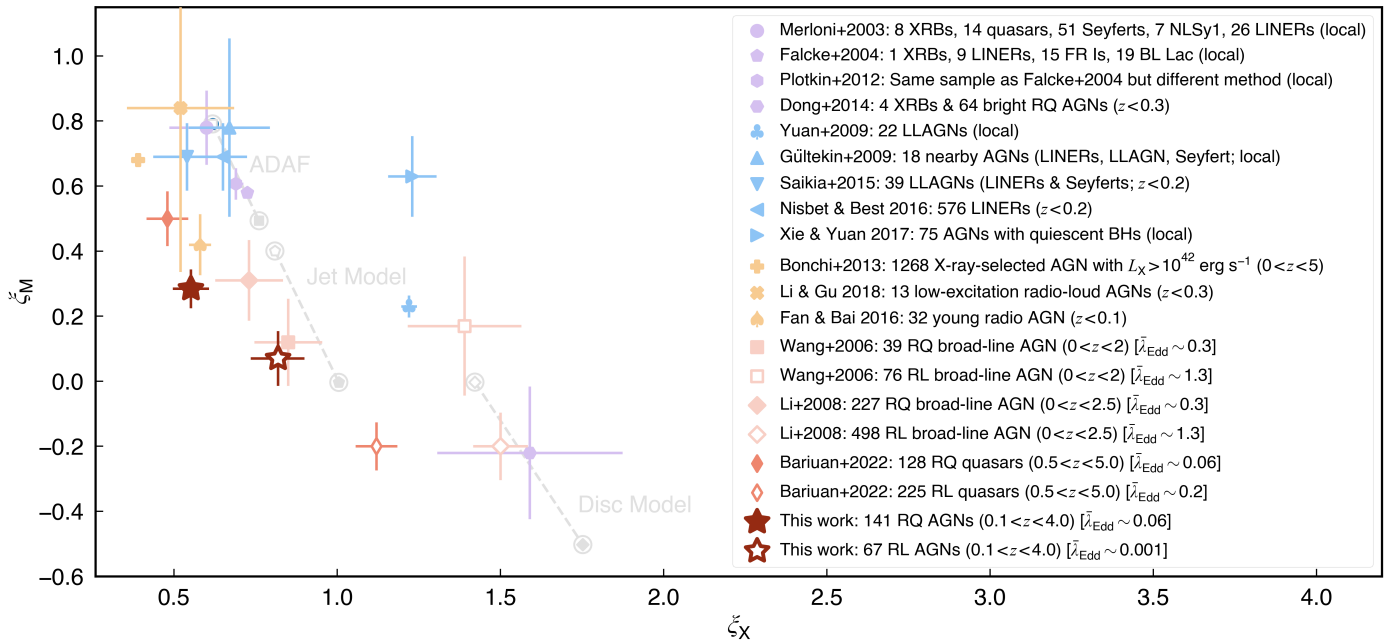


Fig. 4: Comparison of the best-fit correlation coefficients ξ_X and ξ_M of the fundamental plane. Our results for the radio-quiet (RQ) AGNs and radio-loud (RL) AGNs samples are shown as the dark-red filled star and the dark-red empty star, respectively. The results from literature works are shown as comparisons, including Merloni et al. (2003) (Merloni+2003), Falcke et al. (2004) (Falcke+2004), Plotkin et al. (2012) (Plotkin+2012), Dong et al. (2014) (Dong+2014), Yuan et al. (2009) (Yuan+2009), Gültekin et al. (2009b) (Gültekin+2009), Saikia et al. (2015) (Saikia+2015), Nisbet & Best (2016) (Nisbet & Best 2016), Xie & Yuan (2017) (Xie & Yuan 2017), Bonchi et al. (2013) (Bonchi+2013), Li & Gu (2018) (Li & Gu 2018), Fan & Bai (2016) (Fan & Bai 2016), Wang et al. (2006) (Wang+2006), Li et al. (2008) (Li+2008), Bariuan et al. (2022) (Bariuan+2022). Purple symbols represent studies based on a sample consisting of both X-ray binaries (XRBs) and local AGNs. Blue symbols represent studies based on local low-luminosity AGNs (LLAGNs). Yellow symbols represent studies for other types of AGNs. Red symbols represent studies for radio-quiet (filled symbols) and radio-loud (empty symbols) AGN separately. The theoretically predicted correlation coefficients are derived from Merloni et al. (2003) with the electron spectral index $p = 2$, which are shown as a circle with a square in the center for the advection dominated accretion flow (ADAF), a circle with a pentagon in the center for a synchrotron jet model, and a circle with a diamond in the center for the standard Shakura-Sunyaev disc model. For the theoretically predicted correlation coefficients, empty gray symbols and filled gray symbols represent the predictions based on a radio spectral index of 0 and -0.5 , respectively, and the dashed lines connecting the empty and filled symbols represent the tracks of ξ_X and ξ_M due to the variation of radio spectral index.

6.1. A brief summary about the fundamental plane studies

Merloni et al. (2003), Falcke et al. (2004), Plotkin et al. (2012), and Dong et al. (2014) all studied the fundamental plane based on a sample consisting of both X-ray binaries (XRBs) and local AGNs (see the purple symbols in Fig. 4). Merloni et al. (2003), Falcke et al. (2004), and Plotkin et al. (2012) got a consistent result about the fundamental plane of nearly all types of AGNs but with a primary focus of low-luminosity AGNs (LLAGNs), showing that these populations yield an ADAF model. On the other hand, Dong et al. (2014) showed a significantly different pattern that their bright AGNs with higher Eddington ratio are in line with the predictions of the disc model. Thus, such a difference indicates that different types of AGNs may have different fundamental plane.

Furthermore, many studies of the fundamental plane only focus on AGNs. Some works studied the fundamental plane of local LLAGNs (Yuan et al. 2009; Gültekin et al. 2009a; Saikia et al. 2015; Nisbet & Best 2016; Xie & Yuan 2017, see blue symbols in Fig. 4). Gültekin et al. (2009a), Saikia et al. (2015), and Nisbet & Best (2016) obtained consistent results (ADAF model) with those in Merloni et al. (2003) and Falcke et al. (2004), while Yuan et al. (2009) and Xie & Yuan (2017) exhibited different re-

sults. The LLAGNs samples in Gültekin et al. (2009a), Saikia et al. (2015), and Nisbet & Best (2016) have relatively higher Eddington ratio than those in Yuan et al. (2009) and Xie & Yuan (2017), which might explain the different results among them. In addition, X-ray-selected AGN ($L_X > 10^{42}$ erg s $^{-1}$) (Bonchi et al. 2013), low-excitation radio-loud AGN (Li & Gu 2018), and young radio AGNs (Fan & Bai 2016) show a similar fundamental plane with LLAGNs (see yellow symbols in Fig. 4).

In addition, many works explore the fundamental plane of radio-quiet and radio-loud populations separately (Wang et al. 2006; Li et al. 2008; Bariuan et al. 2022). Both Wang et al. (2006) and Li et al. (2008) utilized broad-line AGNs samples and they got a consistent result about the fundamental plane within 1σ uncertainty (see Fig. 4). They all found that radio-quiet and radio-loud AGNs show quite different fundamental planes. Radio-quiet AGNs favor the ADAF model coupled with a synchrotron jet model, while the radio-loud AGNs favor a combination of the disc model with the synchrotron jet model. More recently, Bariuan et al. (2022) found that for luminous quasars, radio-quiet and radio-loud subsets also have different fundamental planes. Therefore, these works demonstrate that the fundamental plane depends on the radio loudness of AGNs.

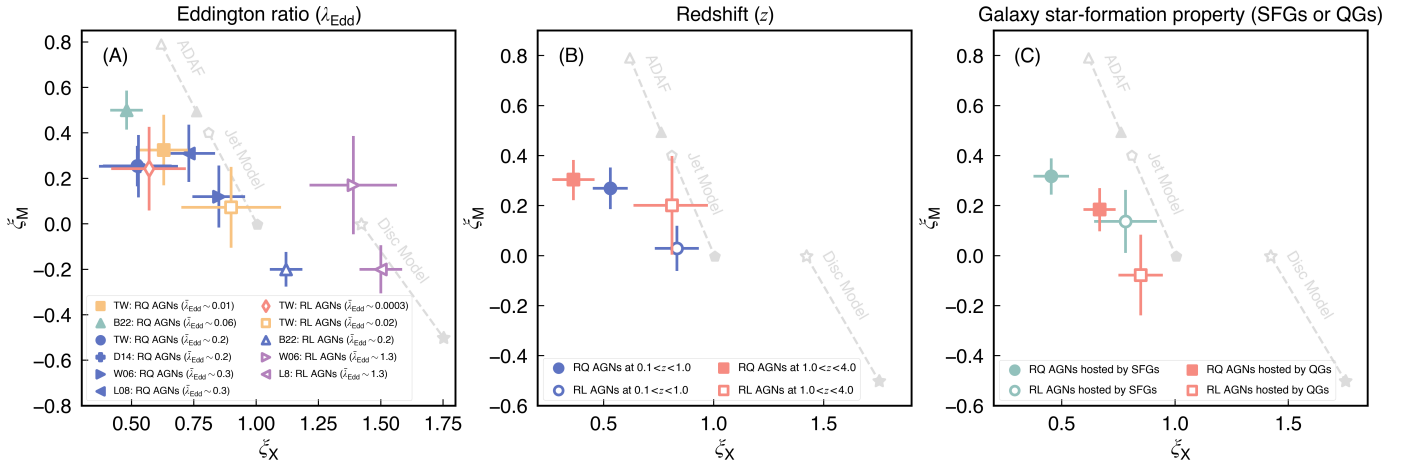


Fig. 5: Comparison of the best-fit correlation coefficients ξ_X and ξ_M of the fundamental plane for Eddington-ratio subsamples (A), redshift subsamples (B), and galaxy-star-formation-property subsamples (C). The theoretically predicted correlation coefficients for ADAF, jet model, and disc model are same as Fig. 4, which are shown here respectively as triangles, pentagons, and stars. In each panel, filled symbols represent radio-quiet (RQ) AGNs and empty symbols represent radio-loud (RL) AGNs. In Panel (A), “TW”, “B22”, “D14”, “W06”, and “L08” means results from this work, Bariuan et al. (2022), Dong et al. (2014), Wang et al. (2006), Li et al. (2008), respectively.

We also separately studied the fundamental plane of radio-quiet and radio-loud AGNs. Comparing to the literature works (Wang et al. 2006; Li et al. 2008; Bariuan et al. 2022), our samples have relatively lower X-ray luminosity, lower radio luminosity, and lower Eddington ratio. We also found that there is a different fundamental plane between radio-quiet and radio-loud AGNs. Our low-luminosity radio-quiet AGNs show a slightly different fundamental plane than the high-luminosity radio-quiet AGNs from Wang et al. (2006), Li et al. (2008), and Bariuan et al. (2022), while our low-luminosity radio-loud AGNs present a significantly different result than the high-luminosity radio-loud AGNs from these literature works (see Fig. 4). These results indicate that the fundamental plane may have a dependence on Eddington ratio (see details in Section 6.2).

6.2. Eddington-ratio dependence for the fundamental plane

We split our radio-quiet AGN subsample into two Eddington-ratio subsets: $\lambda_{\text{Edd}} \leq 10^{-1.5}$ (with a median value of 0.01) and $\lambda_{\text{Edd}} > 10^{-1.5}$ (with a median value of 0.2). Our radio-loud AGN subsample was split into two Eddington-ratio subsets: $\lambda_{\text{Edd}} \leq 10^{-2.5}$ (with a median value of 0.0003) and $\lambda_{\text{Edd}} > 10^{-2.5}$ (with a median value of 0.02). The best-fit parameters for the fundamental plane of these subsets and the source number in each subset are summarized in Table 1. The comparison between ξ_X and ξ_M is shown in Panel A of Fig. 5. For the radio-quiet AGN sample, both the low-Eddington-ratio subset ($\lambda_{\text{Edd}} \leq 10^{-1.5}$; the yellow filled square in Panel A of Fig. 5) and high-Eddington-ratio subset ($\lambda_{\text{Edd}} > 10^{-1.5}$; the blue filled circle in Panel A of Fig. 5) agree with an ADAF model coupled with a synchrotron jet model. For the radio-loud AGN sample, the low-Eddington-ratio subset ($\lambda_{\text{Edd}} \leq 10^{-2.5}$; the red empty diamond in Panel A of Fig. 5) can be explained by an ADAF model coupled with a jet model, while the high-Eddington-ratio subset ($\lambda_{\text{Edd}} > 10^{-2.5}$; the yellow empty square in Panel A of Fig. 5) mainly follows a jet model. For comparison, ξ_X and ξ_M from Wang et al. (2006) (W06), Li et al. (2008) (L08), and Bariuan et al. (2022) (B22) are shown in Panel A of Fig. 5. In addition, we also analyzed the fundamental plane for the radio-quiet AGN sample from Dong

et al. (2014) (D14) whose best-fit parameters are also shown in Panel A of Fig. 5. Our samples and samples from these literature works have different Eddington ratio and follow different fundamental planes (see Panel A of Fig. 5). According to these results, we found that for both radio-quiet AGNs and radio-loud AGNs, their fundamental planes may depend on Eddington ratio.

6.3. Redshift dependence for the fundamental plane

We further studied the fundamental plane of radio-quiet and radio-loud AGN subsamples by splitting them into two redshift subsets: $0.1 < z \leq 1$ and $1 < z \leq 4$. For each subset, the best-fit parameters and source numbers are summarized in Table 1. For both radio-loud AGNs and radio-quiet AGNs, there seems to be no significant redshift dependence for the fundamental plane (see Panel B of Fig. 5). For luminous AGNs (such as broad-line AGNs and quasars), Li et al. (2008) found no significant dependence on redshift for both radio-quiet and radio-loud subsets across $0 < z < 2.5$, while Bariuan et al. (2022) only observed a redshift dependence for radio-loud subset across $0.1 < z < 5$. In the future, larger samples across a broad luminosity range and a wide redshift range are required to draw a firm conclusion about the redshift dependence.

6.4. Galaxy-star-formation-property dependence for the fundamental plane

For the first time, we studied the galaxy-star-formation-property (SFGs and QGs) dependence for the fundamental plane whose best-fit parameters and source numbers are summarized in Table 1. We adopted the UVJ selection criteria in Schreiber et al. (2015) to decide galaxy types (SFG or QG). Here the UVJ magnitudes of our sample were derived from literature works (GOODS-N: Barro et al. 2019; GOODS-S: Straatman et al. 2016; COSMOS: Weaver et al. 2022). Radio AGNs hosted by SFGs and QGs have different cosmic evolutions for AGN incident rate (e.g., Janssen et al. 2012; Kondapally et al. 2022, Paper I) and radio luminosity functions (Kondapally et al. 2022, Paper I). In addition, SFGs and QGs have different gas contents

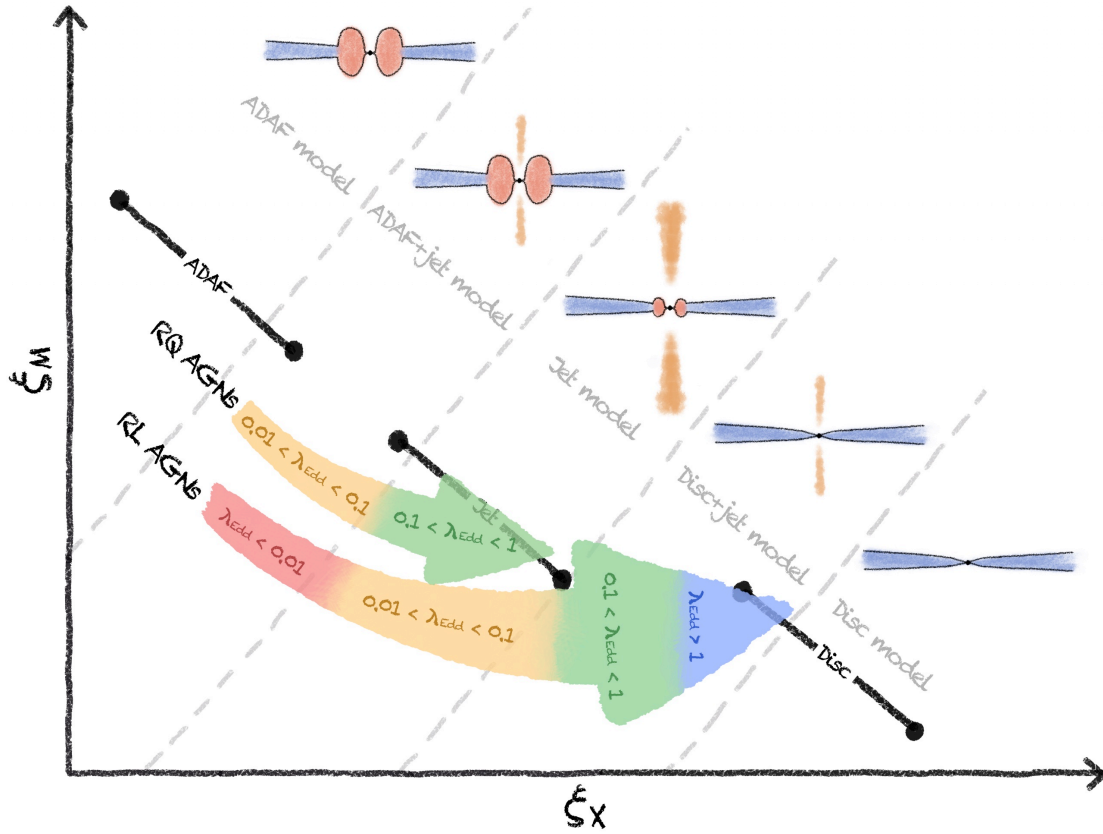


Fig. 6: Cartoon illustrating the model for the central engine of radio-quiet AGNs and radio-loud AGNs. Black solid lines represent the theoretically predicted correlation coefficients for ADAF, jet, and standard thin disc models, which are same as Fig. 4 and Fig. 5. The upper colored arrow represents the observational results for radio-quiet (RQ) AGNs, while the lower colored arrow represents the observational results for radio-loud (RL) AGNs. The different colors of the arrow represent different Eddington ratio (λ_{Edd}) and the direction of the arrow means from low λ_{Edd} to high λ_{Edd} . Radio-quiet AGNs at $0.01 < \lambda_{\text{Edd}} < 0.1$ are consistent with a combination of ADAF and a synchrotron jet model (ADAF+jet model), while at $0.1 < \lambda_{\text{Edd}} < 1$, they mainly follow the synchrotron jet model (Jet model). Radio-loud AGNs are consistent with a combination of ADAF and a synchrotron jet model (ADAF+jet model) at $\lambda_{\text{Edd}} < 0.01$, and agree with the synchrotron jet model (Jet model) at $0.01 < \lambda_{\text{Edd}} < 0.1$, and follow the standard thin disc coupled with a jet model (Disc+jet model) at $\lambda_{\text{Edd}} > 0.1$.

that may perform different fueling mechanisms toward central SMBHs (e.g., [Kauffmann & Heckman 2009](#); [Kondapally et al. 2022](#); [Ni et al. 2023](#)). However, as Panel (C) of Fig. 5 shows, neither the radio-loud AGNs nor the radio-quiet AGNs show a significant dependence on the galaxy star-formation properties, which indicates that galaxy star-formation properties may not a major factor to affect the fundamental plane and the disc-jet connection may not depend on the fueling mechanisms of host galaxies. In addition, nearly 82% of radio-quiet AGNs are hosted by SFGs and 18% of the radio-quiet AGNs are hosted by QGs (see Table 1 and Panel B of Fig. 1), while the fraction of the radio-loud AGNs hosted by SFGs and QGs are both around 50% (see Table 1 and Panel C of Fig. 1).

6.5. Central engine for radio-quiet and radio-loud AGNs

As we mentioned in Section 6.1, radio-quiet AGNs and radio-loud AGNs are found to follow different fundamental planes, which may correspond to different accretion physics for the central engine (see Fig. 4). In Fig. 6, we show a cartoon illustrating the central engines of radio-quiet AGNs and radio-loud AGNs based on the observational results.

According to the observational evidences from our work and literature works (see details in Section 6.2), radio-quiet AGNs at $0.01 < \lambda_{\text{Edd}} < 0.1$ are consistent with a combination of ADAF and a synchrotron jet model, while at $0.1 < \lambda_{\text{Edd}} < 1$, they mainly follow the synchrotron jet model (see Panel A in Fig. 5 or the cartoon illustration in Fig. 6). For radio-quiet AGNs at other λ_{Edd} ranges, more observational data are required to verify this trend in the future. [Wang et al. \(2022a\)](#) studied the ambient circumnuclear medium of six radio-quiet AGNs with $0.05 < \lambda_{\text{Edd}} < 0.5$ based on the high-resolution X-ray analysis for warm absorber outflows. The density profile of the ambient circumnuclear medium shows that for these six radio-quiet AGNs, the accretion physics from 0.01 parsec to a few parsec (corresponding to a physical scale from the broad-line region to the torus; [Wang et al. 2022b](#)) are consistent with the standard thin disc model. One possible reason for the difference between this work and [Wang et al. \(2022a\)](#) is that for different physical scales. The fundamental plane describes the disc-jet or corona-jet connection in the innermost region of the accretion flow ([Merloni et al. 2003](#)), which reflects the accretion physics around several Schwarzschild radius (e.g., [Alston et al. 2020](#)) (corresponding to about 10^{-4} parsec assuming a $10^8 M_{\odot}$ black hole). Thus, the physical scale we target in this work is much smaller than that in [Wang et al. \(2022a\)](#).

Radio-loud AGNs are consistent with a combination of ADAF and a synchrotron jet model at $\lambda_{\text{Edd}} < 0.01$, and agree with the synchrotron jet model at $0.01 < \lambda_{\text{Edd}} < 0.1$, and follow the standard thin disc coupled with a jet model at $\lambda_{\text{Edd}} > 0.1$ (see Panel A in Fig. 5 or the cartoon illustration in Fig. 6). The result for the high- λ_{Edd} radio-loud AGN is consistent with that in Zhong et al. (2023) who found that the extremely powerful radio jets are a result of either the spectral transition from ADAF to a thin disc or a super-Eddington accretion.

7. Summary and conclusions

We investigated the fundamental plane of black hole activity based on a large radio AGN sample selected from the GOODS-N, the GOODS-S, and the COSMOS/UltraVISTA fields across $0.1 < z \leq 4$. This radio AGN sample consists of 208 objects with available estimates for rest-frame 5 GHz radio luminosity (L_R) and rest-frame 2–10 keV X-ray luminosity (L_X), and inferred black hole mass (M_{BH}) from stellar mass (Section 3). Then we divided this radio AGN sample into 141 radio-quiet AGNs and 67 radio-loud AGNs (Section 4), and studied their fundamental planes separately (Section 5). Further, we summarized the current studies about the fundamental plane (Section 6.1). Finally, we explored the dependence of the fundamental plane on Eddington ratio (Section 6.2), redshift (Section 6.3), and galaxy star-formation properties (Section 6.4), and discussed the central engines of radio-quiet and radio-loud AGNs (Section 6.5). The main conclusions are shown as follows:

- (i) The ratio of L_R to L_X , also known as a tracer for radio-loudness, shows a bimodal distribution which can be well described by two single Gaussian models (Fig. 1). The cross point between these two Gaussian components, that is $\log(L_R/L_X) = -2.73$, is defined as a radio-loudness threshold to divide radio-quiet and radio-loud AGN in this work.
- (ii) Our Radio-quiet AGNs have larger X-ray luminosity, lower radio luminosity, and significantly larger Eddington ratio comparing to our radio-loud AGNs.
- (iii) Our radio-quiet and radio-loud AGNs show significantly different fundamental plane which is $\log L_R = (0.55 \pm 0.05) \log L_X + (0.28 \pm 0.06) \log M_{\text{BH}} + (13.54 \pm 2.27)$ for the radio-quiet AGNs, and $\log L_R = (0.82 \pm 0.08) \log L_X + (0.07 \pm 0.08) \log M_{\text{BH}} + (5.24 \pm 3.33)$ for the radio-loud AGNs (Fig. 3 and Table A1). Our radio-quiet AGNs can be explained by an ADAF model coupled with a synchrotron jet model, while our radio-loud AGNs mainly agree with a synchrotron emitting jet model (Fig. 4).
- (iv) For both radio-quiet and radio-loud AGNs, the fundamental plane shows a significant dependence on Eddington ratio (Panel A in Fig. 5), while it presents no significant dependence on redshift and galaxy star-formation properties (SFGs and QGs) (Panels B and C in Fig. 5, respectively).
- (v) Radio-quiet and radio-loud AGNs at different accretion states have different fundamental planes (Fig. 4) corresponding to different central engines (Fig. 6). Radio-quiet AGNs at $0.01 < \lambda_{\text{Edd}} < 0.1$ are consistent with a combination of ADAF and a synchrotron jet model, while at $0.1 < \lambda_{\text{Edd}} < 1$, they mainly follow the synchrotron jet model (Fig. 6). Radio-loud AGNs are consistent with a combination of ADAF and a synchrotron jet model at $\lambda_{\text{Edd}} < 0.01$, and agree with the synchrotron jet model at $0.01 < \lambda_{\text{Edd}} < 0.1$, and follow the standard thin disc coupled with the jet model at $\lambda_{\text{Edd}} > 0.1$ (Fig. 6).

Acknowledgements. We thank Stefano Marchesi and Giorgio Lanzuisi for kind help to access the COSMOS-Legacy survey data. This work is supported by the National Natural Science Foundation of China (Project No. 12173017 and Key Project No. 12141301). LCH was supported by the National Science Foundation of China (11991052, 12011540375, 12233001), the National Key R&D Program of China (2022YFF0503401), and the China Manned Space Project (CMS-CSST-2021-A04, CMS-CSST-2021-A06).

References

- Aird, J., Nandra, K., Laird, E. S., et al. 2010, *MNRAS*, 401, 2531
- Alberts, S., Rujopakarn, W., Rieke, G. H., Jagannathan, P., & Nyland, K. 2020, *ApJ*, 901, 168
- Alston, W. N., Fabian, A. C., Kara, E., et al. 2020, *Nature Astronomy*, 4, 597
- Bariuan, L. G. C., Snios, B., Sobolewska, M., Siemiginowska, A., & Schwartz, D. A. 2022, *MNRAS*, 513, 4673
- Barro, G., Pérez-González, P. G., Cava, A., et al. 2019, *ApJS*, 243, 22
- Begelman, M. C., Blandford, R. D., & Rees, M. J. 1984, *Reviews of Modern Physics*, 56, 255
- Bell, E. F., McIntosh, D. H., Katz, N., & Weinberg, M. D. 2003, *ApJS*, 149, 289
- Bonchi, A., La Franca, F., Melini, G., Bongiorno, A., & Fiore, F. 2013, *MNRAS*, 429, 1970
- Boquien, M., Burgarella, D., Roehlly, Y., et al. 2019, *A&A*, 622, A103
- Burgarella, D., Buat, V., & Iglesias-Páramo, J. 2005, *MNRAS*, 360, 1413
- Chabrier, G. 2003, *ApJ*, 586, L133
- Civano, F., Marchesi, S., Comastri, A., et al. 2016, *ApJ*, 819, 62
- Condon, J. J. 1992, *ARA&A*, 30, 575
- Cowie, L. L., González-López, J., Barger, A. J., et al. 2018, *ApJ*, 865, 106
- de Gasperin, F., Intema, H. T., & Frail, D. A. 2018, *MNRAS*, 474, 5008
- Delhaize, J., Smolčić, V., Delvecchio, I., et al. 2017, *A&A*, 602, A4
- Delvecchio, I., Daddi, E., Sargent, M. T., et al. 2022, *A&A*, 668, A81
- Done, C. & Gierliński, M. 2005, *MNRAS*, 364, 208
- Dong, A.-J., Wu, Q., & Cao, X.-F. 2014, *ApJ*, 787, L20
- Dubner, G. & Giacani, E. 2015, *A&A Rev.*, 23, 3
- Duras, F., Bongiorno, A., Ricci, F., et al. 2020, *A&A*, 636, A73
- Enia, A., Talia, M., Pozzi, F., et al. 2022, *ApJ*, 927, 204
- Fabian, A. C. 2012, *ARA&A*, 50, 455
- Falcke, H., Kording, E., & Markoff, S. 2004, *A&A*, 414, 895
- Fan, X.-L. & Bai, J.-M. 2016, *ApJ*, 818, 185
- Gómez-Guijarro, C., Elbaz, D., Xiao, M., et al. 2022, *A&A*, 658, A43
- Greene, J. E., Strader, J., & Ho, L. C. 2020, *ARA&A*, 58, 257
- Grimm, H. J., Gilfanov, M., & Sunyaev, R. 2003, *MNRAS*, 339, 793
- Gültekin, K., Cackett, E. M., Miller, J. M., et al. 2009a, *ApJ*, 706, 404
- Gültekin, K., Richstone, D. O., Gebhardt, K., et al. 2009b, *ApJ*, 698, 198
- Guo, Y., Ferguson, H. C., Gialalisco, M., et al. 2013, *ApJS*, 207, 24
- Haardt, F. & Maraschi, L. 1991, *ApJ*, 380, L51
- Helou, G., Soifer, B. T., & Rowan-Robinson, M. 1985, *ApJ*, 298, L7
- Ho, L. C. 2002, *ApJ*, 564, 120
- Ho, L. C. 2008, *ARA&A*, 46, 475
- Janssen, R. M. J., Röttgering, H. J. A., Best, P. N., & Brinchmann, J. 2012, *A&A*, 541, A62
- Jin, S., Daddi, E., Liu, D., et al. 2018, *ApJ*, 864, 56
- Kauffmann, G. & Heckman, T. M. 2009, *MNRAS*, 397, 135
- King, A. & Pounds, K. 2015, *ARA&A*, 53, 115
- Kondapally, R., Best, P. N., Cochrane, R. K., et al. 2022, *MNRAS*, 513, 3742
- Körding, E. 2014, *Space Sci. Rev.*, 183, 149
- Kroupa, P. 2001, *MNRAS*, 322, 231
- Lanzuisi, G., Civano, F., Marchesi, S., et al. 2018, *MNRAS*, 480, 2578
- Lehmer, B. D., Alexander, D. M., Bauer, F. E., et al. 2010, *ApJ*, 724, 559
- Lehmer, B. D., Basu-Zych, A. R., Mineo, S., et al. 2016, *ApJ*, 825, 7
- Li, J., Xue, Y., Sun, M., et al. 2019, *ApJ*, 877, 5
- Li, J. I. H., Shen, Y., Ho, L. C., et al. 2023, *ApJ*, 954, 173
- Li, S.-L. & Gu, M. 2018, *MNRAS*, 481, L45
- Li, Z.-Y., Wu, X.-B., & Wang, R. 2008, *ApJ*, 688, 826
- Liu, B. F. & Qiao, E. 2022, *iScience*, 25, 103544
- Liu, D., Daddi, E., Dickinson, M., et al. 2018, *ApJ*, 853, 172
- Liu, T., Tozzi, P., Wang, J.-X., et al. 2017, *ApJS*, 232, 8
- Luo, B., Brandt, W. N., Xue, Y. Q., et al. 2017, *ApJS*, 228, 2
- Lyu, J., Alberts, S., Rieke, G. H., & Rujopakarn, W. 2022, *ApJ*, 941, 191
- Madau, P. & Dickinson, M. 2014, *ARA&A*, 52, 415
- Magnelli, B., Ivison, R. J., Lutz, D., et al. 2015, *A&A*, 573, A45
- Marchesi, S., Lanzuisi, G., Civano, F., et al. 2016, *ApJ*, 830, 100
- McHardy, I. M., Koerding, E., Knigge, C., Uttley, P., & Fender, R. P. 2006, *Nature*, 444, 730
- Merloni, A., Heinz, S., & di Matteo, T. 2003, *MNRAS*, 345, 1057
- Mineo, S., Gilfanov, M., Lehmer, B. D., Morrison, G. E., & Sunyaev, R. 2014, *MNRAS*, 437, 1698
- Mineo, S., Gilfanov, M., & Sunyaev, R. 2012, *MNRAS*, 419, 2095

- Murphy, E. J., Momjian, E., Condon, J. J., et al. 2017, *ApJ*, 839, 35
- Narayan, R. & Yi, I. 1994, *ApJ*, 428, L13
- Ni, Q., Aird, J., Merloni, A., et al. 2023, *MNRAS*[arXiv:2307.00051]
- Nisbet, D. M. & Best, P. N. 2016, *MNRAS*, 455, 2551
- Noll, S., Burgarella, D., Giovannoli, E., et al. 2009, *A&A*, 507, 1793
- Novak, M., Smolčić, V., Delhaize, J., et al. 2017, *A&A*, 602, A5
- Owen, F. N. 2018, *ApJS*, 235, 34
- Panessa, F., Baldi, R. D., Laor, A., et al. 2019, *Nature Astronomy*, 3, 387
- Panessa, F., Barcons, X., Bassani, L., et al. 2007, *A&A*, 467, 519
- Pedregosa, F., Varoquaux, G., Gramfort, A., et al. 2011, *Journal of Machine Learning Research*, 12, 2825
- Plotkin, R. M., Markoff, S., Kelly, B. C., Körding, E., & Anderson, S. F. 2012, *MNRAS*, 419, 267
- Pringle, J. E. 1981, *ARA&A*, 19, 137
- Ruan, J. J., Anderson, S. F., Eracleous, M., et al. 2019, *ApJ*, 883, 76
- Rybicki, G. B. & Lightman, A. P. 1979, *Astronomy Quarterly*, 3, 199
- Saikia, P., Körding, E., & Falcke, H. 2015, *MNRAS*, 450, 2317
- Schreiber, C., Pannella, M., Elbaz, D., et al. 2015, *A&A*, 575, A74
- Shakura, N. I. & Sunyaev, R. A. 1973, *A&A*, 24, 337
- Sikora, M., Stawarz, Ł., & Lasota, J.-P. 2007, *ApJ*, 658, 815
- Smolčić, V., Novak, M., Bondi, M., et al. 2017, *A&A*, 602, A1
- Speagle, J. S., Steinhardt, C. L., Capak, P. L., & Silverman, J. D. 2014, *ApJS*, 214, 15
- Straatman, C. M. S., Spitler, L. R., Quadri, R. F., et al. 2016, *ApJ*, 830, 51
- Tadaki, K.-i., Belli, S., Burkert, A., et al. 2020, *ApJ*, 901, 74
- Terashima, Y. & Wilson, A. S. 2003, *ApJ*, 583, 145
- Tozzi, P., Gilli, R., Mainieri, V., et al. 2006, *A&A*, 451, 457
- van der Wel, A., Holden, B. P., Franx, M., et al. 2007, *ApJ*, 670, 206
- Wang, R., Wu, X.-B., & Kong, M.-Z. 2006, *ApJ*, 645, 890
- Wang, Y., He, Z., Mao, J., et al. 2022a, *ApJ*, 928, 7
- Wang, Y., Kaastra, J., Mehdipour, M., et al. 2022b, *A&A*, 657, A77
- Wang, Y., Wang, T., Liu, D., et al. 2024, *arXiv e-prints*, arXiv:2401.04924
- Weaver, J. R., Kauffmann, O. B., Ilbert, O., et al. 2022, *ApJS*, 258, 11
- Xie, F.-G. & Yuan, F. 2017, *ApJ*, 836, 104
- Xue, Y. Q., Luo, B., Brandt, W. N., et al. 2016, *ApJS*, 224, 15
- Yang, G., Boquien, M., Brandt, W. N., et al. 2022, *ApJ*, 927, 192
- Yang, G., Boquien, M., Buat, V., et al. 2020, *MNRAS*, 491, 740
- Yuan, F. 2001, *MNRAS*, 324, 119
- Yuan, F. & Narayan, R. 2014, *ARA&A*, 52, 529
- Yuan, F., Yu, Z., & Ho, L. C. 2009, *ApJ*, 703, 1034
- Zhong, Y., Inoue, A. K., Sugahara, Y., et al. 2023, *arXiv e-prints*, arXiv:2312.09649

Table A1: Radio AGN sample used in the analysis for the fundamental plane of black hole activity. (1) Survey name: “GOODSN” for the GOODS-N field, “GOODSS” for the GOODS-S field, “COSMOS” for the COSMOS/UltraVISTA field; (2) ID from [Liu et al. \(2018\)](#) (or [Barro et al. 2019](#)) for the GOODS-N, from [Guo et al. \(2013\)](#) for the GOODS-S, from [Jin et al. \(2018\)](#) for the COSMOS; (3) Right Ascension; (4) Declination; (5) Redshift; (6) Radio-loudness type: “RQ” for radio-quiet AGN, “RL” for radio-loud AGN; (7) Rest-frame 5 GHz radio luminosity from AGN; (8) Rest-frame 2–10 keV X-ray luminosity from AGN; (9) Black hole mass inferred from stellar mass; (10) Eddington ratio; (11) Host galaxy star-formation properties: “SFG” for star-forming galaxy, “QG” for quiescent galaxy; (12) Specific star formation rate.

Survey	ID	R.A.	Decl.	z	Type	$\log\left(\frac{L_R}{\text{erg s}^{-1}}\right)$	$\log\left(\frac{L_X}{\text{erg s}^{-1}}\right)$	$\log\left(\frac{M_{\text{BH}}}{M_\odot}\right)$	$\log \lambda_{\text{Edd}}$	Host galaxy	$\log\left(\frac{s\text{SFR}}{\text{Gyr}^{-1}}\right)$
(1)	(2)	(3)	(4)	(5)	(6)	(7)	(8)	(9)	(10)	(11)	(12)
GOODSN	90	189.069981	62.104166	1.141	RQ	39.81 ± 0.05	42.72 ± 0.14	8.51 ± 0.12	-2.61	SFG	-106.78
GOODSN	896	189.206901	62.127243	1.610	RQ	40.47 ± 0.02	44.56 ± 0.01	7.03 ± 0.14	0.72	SFG	0.90
GOODSN	1211	189.135673	62.133290	1.994	RQ	40.42 ± 0.03	43.52 ± 0.05	5.54 ± 0.26	1.17	SFG	2.03
GOODSN	1464	189.312283	62.139902	0.825	RL	41.11 ± 0.01	42.10 ± 0.14	6.81 ± 0.16	-1.52	QG	0.40
GOODSN	2085	189.289291	62.143789	0.907	RL	40.19 ± 0.01	42.33 ± 0.07	8.93 ± 0.13	-3.41	QG	-2.06
GOODSN	2351	189.050155	62.149980	2.220	RQ	40.13 ± 0.10	43.37 ± 0.07	8.62 ± 0.12	-2.07	SFG	-1.22
GOODSN	2955	189.125229	62.156647	0.954	RQ	39.51 ± 0.03	43.10 ± 0.05	7.10 ± 0.14	-0.81	QG	-4.67
GOODSN	3629	189.065078	62.162943	1.263	RL	39.70 ± 0.06	42.11 ± 0.19	8.75 ± 0.12	-3.45	SFG	-0.79
GOODSN	3919	189.027641	62.164241	0.638	RQ	39.76 ± 0.03	43.57 ± 0.05	8.23 ± 0.10	-1.48	SFG	-1.09
GOODSN	4316	189.071192	62.169817	0.846	RQ	39.46 ± 0.05	43.08 ± 0.02	8.16 ± 0.10	-1.89	SFG	-0.89
GOODSN	4345	189.049043	62.170740	0.851	RQ	39.15 ± 0.06	44.12 ± 0.05	7.51 ± 0.11	-0.21	SFG	-0.35
GOODSN	4593	189.062576	62.172613	2.505	RQ	40.71 ± 0.02	43.92 ± 0.11	9.00 ± 0.14	-1.90	QG	-1.70
GOODSN	4663	189.114607	62.173937	0.761	RQ	38.82 ± 0.09	42.92 ± 0.04	7.27 ± 0.11	-1.17	SFG	-1.22
GOODSN	5157	189.033868	62.176641	0.679	RQ	39.95 ± 0.01	43.05 ± 0.05	7.97 ± 0.09	-1.73	QG	-4.87
GOODSN	5195	189.341015	62.176583	0.979	RQ	39.61 ± 0.06	43.51 ± 0.05	8.54 ± 0.11	-1.85	SFG	-0.82
GOODSN	6135	189.066879	62.185503	1.619	RQ	39.74 ± 0.06	44.35 ± 0.01	7.86 ± 0.12	-0.32	SFG	-1.06
GOODSN	6226	189.179527	62.185702	3.230	RQ	37.85 ± 0.07	43.16 ± 0.09	5.39 ± 0.25	0.96	SFG	-2.72
GOODSN	6694	189.135303	62.184818	0.519	RL	38.87 ± 0.07	40.70 ± 0.35	8.66 ± 0.12	-4.78	QG	-2.99
GOODSN	8109	189.266607	62.199309	3.406	RQ	40.59 ± 0.04	44.44 ± 0.11	8.07 ± 0.10	-0.44	QG	-1.00
GOODSN	8513	189.420565	62.200105	1.168	RQ	39.90 ± 0.06	44.05 ± 0.01	8.77 ± 0.13	-1.53	SFG	-0.36
GOODSN	11541	189.153773	62.222334	3.110	RQ	40.57 ± 0.05	44.22 ± 0.10	8.07 ± 0.10	-0.66	SFG	0.56
GOODSN	11561	189.200329	62.219182	0.475	RQ	38.45 ± 0.07	41.57 ± 0.05	8.03 ± 0.10	-3.28	QG	-4.05
GOODSN	11595	189.231040	62.219797	0.955	RQ	39.39 ± 0.04	42.61 ± 0.04	8.60 ± 0.11	-2.80	QG	-2.73
GOODSN	12953	189.073650	62.228983	0.534	RQ	38.50 ± 0.08	41.69 ± 0.11	8.15 ± 0.10	-3.27	QG	-2.84
GOODSN	13456	189.351104	62.233248	0.474	RQ	39.71 ± 0.07	42.72 ± 0.02	7.90 ± 0.10	-2.00	SFG	-4.46
GOODSN	14007	189.193116	62.234636	0.961	RQ	40.38 ± 0.02	43.97 ± 0.01	8.63 ± 0.12	-1.47	SFG	-1.43
GOODSN	14094	189.426126	62.238412	1.554	RL	39.95 ± 0.04	42.41 ± 0.15	7.49 ± 0.10	-1.89	SFG	-0.74
GOODSN	14559	189.403676	62.241388	2.158	RQ	40.44 ± 0.03	44.53 ± 0.02	8.05 ± 0.11	-0.33	SFG	-0.32
GOODSN	16450	189.220352	62.245578	0.321	RL	39.22 ± 0.02	40.81 ± 0.08	8.53 ± 0.11	-4.53	QG	-3.38
GOODSN	16517	188.989304	62.254510	2.423	RQ	39.88 ± 0.10	44.12 ± 0.05	8.16 ± 0.10	-0.85	SFG	0.06
GOODSN	16574	189.065980	62.254315	2.690	RQ	40.18 ± 0.07	44.46 ± 0.06	8.89 ± 0.13	-1.25	SFG	-2.45
GOODSN	17162	189.095584	62.257403	2.583	RQ	40.43 ± 0.03	44.76 ± 0.01	6.66 ± 0.21	1.29	SFG	2.02
GOODSN	17217	189.318220	62.253422	0.559	RL	39.67 ± 0.01	41.33 ± 0.12	8.56 ± 0.11	-4.04	QG	-1.76
GOODSN	17242	189.334881	62.256554	0.937	RL	39.14 ± 0.07	41.82 ± 0.15	8.60 ± 0.11	-3.59	QG	-2.66
GOODSN	18204	189.175812	62.262626	0.858	RQ	39.94 ± 0.03	42.85 ± 0.03	8.51 ± 0.11	-2.48	SFG	-0.72
GOODSN	18583	189.270299	62.267106	1.890	RQ	39.91 ± 0.06	44.20 ± 0.01	8.11 ± 0.10	-0.73	SFG	-0.31
GOODSN	22096	189.543917	62.291455	1.256	RQ	39.83 ± 0.07	44.18 ± 0.02	8.26 ± 0.10	-0.89	QG	-6.93
GOODSN	22224	189.319477	62.292585	1.146	RQ	40.12 ± 0.01	44.11 ± 0.01	7.48 ± 0.11	-0.18	SFG	-0.41
GOODSN	23451	189.393419	62.303323	2.241	RQ	39.99 ± 0.07	43.22 ± 0.12	8.41 ± 0.11	-1.99	QG	-1.66
GOODSN	23652	189.247165	62.309045	2.199	RL	42.39 ± 0.01	43.60 ± 0.06	8.37 ± 0.10	-1.59	QG	-5.90
GOODSN	23856	189.254555	62.352667	0.800	RL	40.34 ± 0.01	41.99 ± 0.15	8.82 ± 0.13	-3.64	QG	-6.10
GOODSN	24659	189.413983	62.350082	0.837	RQ	39.55 ± 0.05	43.87 ± 0.01	5.35 ± 0.27	1.71	QG	1.75
GOODSN	24879	189.281190	62.363283	1.450	RQ	39.90 ± 0.08	44.35 ± 0.01	8.56 ± 0.12	-1.03	SFG	-0.34
GOODSN	25194	189.256368	62.340213	2.990	RQ	40.69 ± 0.04	44.05 ± 0.12	8.88 ± 0.13	-1.64	SFG	-0.06
GOODSN	27062	189.324500	62.315479	2.237	RQ	39.95 ± 0.07	44.34 ± 0.01	7.30 ± 0.14	0.22	SFG	0.84
GOODSN	27423	189.168911	62.309187	1.146	RL	40.61 ± 0.01	41.82 ± 0.20	8.61 ± 0.11	-3.60	SFG	-1.93
GOODSS	25734	53.111521	-27.695987	0.734	RQ	39.22 ± 0.07	42.95 ± 0.04	8.22 ± 0.13	-2.09	SFG	-0.92
GOODSS	25273	53.101073	-27.690674	0.534	RQ	38.99 ± 0.04	42.59 ± 0.03	8.57 ± 0.13	-2.79	QG	-2.78
GOODSS	24497	53.110392	-27.676539	1.031	RQ	39.48 ± 0.09	43.98 ± 0.02	6.85 ± 0.17	0.32	SFG	1.39
GOODSS	24012	53.174944	-27.663675	0.152	RL	38.86 ± 0.03	40.46 ± 0.13	7.72 ± 0.13	-4.08	QG	-1.20
GOODSS	23922	53.167050	-27.659599	0.733	RQ	39.23 ± 0.08	43.38 ± 0.05	8.18 ± 0.10	-1.61	QG	-5.86
GOODSS	23259	53.040437	-27.713362	0.733	RL	40.33 ± 0.01	42.18 ± 0.04	8.95 ± 0.14	-3.58	QG	-2.78
GOODSS	23153	53.138691	-27.709999	1.213	RQ	39.44 ± 0.07	43.42 ± 0.05	7.49 ± 0.13	-0.88	SFG	-5.86
GOODSS	22879	53.186044	-27.700681	0.709	RL	39.46 ± 0.02	41.41 ± 0.20	8.01 ± 0.10	-3.41	QG	-1.85
GOODSS	20859	53.152971	-27.735114	0.666	RQ	38.74 ± 0.07	42.96 ± 0.02	7.68 ± 0.10	-1.53	SFG	-5.86
GOODSS	20447	53.045478	-27.737492	1.615	RL	41.84 ± 0.00	44.27 ± 0.01	8.97 ± 0.14	-1.51	SFG	-0.92
GOODSS	20219	53.094107	-27.740510	0.738	RQ	39.61 ± 0.05	43.31 ± 0.71	8.35 ± 0.11	-1.86	SFG	-0.30
GOODSS	19892	53.079375	-27.741624	3.356	RL	39.99 ± 0.06	42.27 ± 0.22	8.51 ± 0.13	-3.05	SFG	0.06
GOODSS	18638	53.121828	-27.752702	1.831	RQ	39.67 ± 0.07	42.59 ± 0.19	8.15 ± 0.13	-2.37	SFG	-0.30
GOODSS	18166	53.124914	-27.758302	1.209	RQ	39.43 ± 0.06	43.89 ± 0.02	6.58 ± 3.24	0.49	SFG	1.36
GOODSS	17206	53.015224	-27.767690	0.574	RQ	39.40 ± 0.05	43.09 ± 0.04	8.59 ± 0.12	-2.31	QG	-8.21
GOODSS	16985	53.093923	-27.767722	1.730	RQ	39.73 ± 0.08	43.81 ± 0.05	8.23 ± 0.10	-1.23	SFG	-0.33
GOODSS	16599	53.119720	-27.772304	0.738	RL	40.11 ± 0.01	42.15 ± 0.05	8.35 ± 0.14	-3.01	QG	-18.46
GOODSS	16375	53.044947	-27.774393	1.610	RL	40.82 ± 0.01	42.11 ± 0.10	9.16 ± 0.15	-3.86	QG	-5.86
GOODSS	16274	53.131080	-27.773108	2.220	RL	40.59 ± 0.03	42.93 ± 0.06	8.25 ± 0.27	-2.13	SFG	0.45
GOODSS	15901	53.193097	-27.775562	1.220	RQ	39.38 ± 0.06	43.81 ± 0.04	7.35 ± 0.11	-0.35	SFG	-0.28

Table A1: Radio AGN sample used in the analysis for the fundamental plane (continued).

Survey	ID	R.A.	Decl.	z	Type	$\log\left(\frac{L_R}{\text{erg s}^{-1}}\right)$	$\log\left(\frac{L_X}{\text{erg s}^{-1}}\right)$	$\log\left(\frac{M_{\text{BH}}}{M_\odot}\right)$	$\log \lambda_{\text{Edd}}$	Host galaxy	$\log\left(\frac{\text{sSFR}}{\text{Gyr}}\right)$
(1)	(2)	(3)	(4)	(5)	(6)	(7)	(8)	(9)	(10)	(11)	(12)
GOODSS	15381	53.180515	-27.779666	2.589	RL	40.35 ± 0.03	42.26 ± 0.22	7.96 ± 0.12	-2.52	SFG	0.42
GOODSS	14781	53.033328	-27.782575	2.612	RQ	40.30 ± 0.09	44.15 ± 0.05	8.40 ± 0.11	-1.07	SFG	-0.05
GOODSS	13729	53.036091	-27.792883	0.543	RQ	40.95 ± 0.00	43.89 ± 0.01	8.78 ± 0.12	-1.71	SFG	-0.92
GOODSS	12526	53.108340	-27.797645	1.897	RL	39.99 ± 0.11	42.25 ± 0.19	7.57 ± 0.14	-2.14	SFG	0.59
GOODSS	10578	53.165283	-27.814068	3.064	RQ	40.67 ± 0.02	44.62 ± 0.03	9.00 ± 0.20	-1.19	QG	-1.85
GOODSS	10497	53.181989	-27.814120	2.958	RL	40.63 ± 0.02	42.69 ± 0.16	8.26 ± 0.10	-2.38	SFG	-0.28
GOODSS	10348	53.066754	-27.816593	1.413	RL	39.86 ± 0.05	41.71 ± 0.14	8.33 ± 0.10	-3.43	SFG	-5.86
GOODSS	10014	53.058894	-27.819501	2.076	RL	40.60 ± 0.02	42.53 ± 0.09	7.70 ± 0.17	-1.98	SFG	0.45
GOODSS	8923	53.142844	-27.827890	0.366	RL	38.38 ± 0.05	40.68 ± 0.14	4.28 ± 0.36	-0.42	SFG	0.95
GOODSS	8833	53.030641	-27.828322	3.485	RL	40.80 ± 0.06	43.13 ± 0.07	7.00 ± 0.30	-0.68	SFG	0.00
GOODSS	8758	53.056171	-27.831346	0.731	RL	39.76 ± 0.02	41.67 ± 0.13	8.16 ± 0.10	-3.31	QG	-2.13
GOODSS	7551	53.131435	-27.841327	1.613	RL	40.20 ± 0.02	42.47 ± 0.11	8.82 ± 0.13	-3.16	SFG	-0.30
GOODSS	7442	53.141819	-27.841356	1.384	RL	39.69 ± 0.12	40.62 ± 1.49	8.10 ± 0.11	-4.30	SFG	0.06
GOODSS	7250	53.027374	-27.843922	0.339	RL	38.78 ± 0.11	39.89 ± 0.57	6.80 ± 0.14	-3.73	SFG	-0.05
GOODSS	7061	53.201811	-27.844133	2.661	RL	40.03 ± 0.13	42.07 ± 0.20	7.12 ± 0.31	-1.87	SFG	1.24
GOODSS	6752	53.076400	-27.848664	1.536	RQ	40.04 ± 0.04	44.11 ± 0.04	8.81 ± 0.13	-1.51	QG	-1.85
GOODSS	5893	53.195148	-27.855868	2.292	RQ	39.65 ± 0.04	42.75 ± 0.09	6.49 ± 0.16	-0.56	SFG	1.38
GOODSS	5479	53.078464	-27.859856	3.660	RQ	40.77 ± 0.05	44.11 ± 0.09	8.84 ± 0.13	-1.54	SFG	-0.30
GOODSS	4526	53.157342	-27.870087	1.603	RQ	40.33 ± 0.02	44.35 ± 0.02	9.09 ± 0.14	-1.55	SFG	-0.92
GOODSS	3973	53.139319	-27.874500	3.673	RL	41.14 ± 0.02	43.34 ± 0.08	8.58 ± 0.11	-2.06	QG	-5.86
GOODSS	3188	53.263706	-27.885171	1.346	RL	39.93 ± 0.09	42.66 ± 0.19	8.58 ± 0.11	-2.74	SFG	-1.85
GOODSS	1256	53.104830	-27.913926	1.090	RQ	39.90 ± 0.03	43.33 ± 0.11	8.73 ± 0.12	-2.22	SFG	-2.13
GOODSS	569	53.170144	-27.929655	3.350	RQ	40.13 ± 0.03	44.76 ± 0.04	6.72 ± 0.43	1.22	SFG	1.07
GOODSS	528	53.113470	-27.933294	1.089	RL	39.81 ± 0.07	41.76 ± 0.20	8.67 ± 0.12	-3.72	SFG	-1.85
GOODSS	135	53.142288	-27.944471	2.897	RL	41.39 ± 0.08	43.76 ± 0.12	8.51 ± 0.17	-1.56	SFG	0.87
COSMOS	552411	150.343730	-2.140640	1.787	RQ	40.58 ± 0.03	44.36 ± 0.03	8.90 ± 0.14	-1.36	SFG	0.07
COSMOS	10002464	150.376620	-1.717860	0.655	RQ	39.82 ± 0.03	44.16 ± 0.04	7.20 ± 0.12	0.15	SFG	0.07
COSMOS	10004014	150.671800	-1.760100	1.175	RQ	40.29 ± 0.02	43.95 ± 0.20	8.67 ± 0.13	-1.54	QG	-0.21
COSMOS	10005234	150.478240	-1.790330	0.702	RQ	39.66 ± 0.03	43.45 ± 0.20	8.36 ± 0.11	-1.72	QG	-0.54
COSMOS	10006773	150.661830	-1.833660	1.574	RL	41.48 ± 0.02	43.73 ± 0.20	8.55 ± 0.12	-1.64	QG	-0.20
COSMOS	10009202	150.694850	-1.886880	1.173	RQ	39.93 ± 0.04	44.25 ± 0.20	8.20 ± 0.11	-0.76	SFG	0.17
COSMOS	10009415	150.447070	-1.882840	0.670	RL	40.71 ± 0.02	42.74 ± 0.11	9.46 ± 0.18	-3.53	SFG	-1.83
COSMOS	10012067	150.697430	-1.933730	0.306	RQ	38.60 ± 0.04	42.18 ± 0.20	7.90 ± 0.11	-2.54	QG	-1.38
COSMOS	10012117	150.467640	-1.935740	0.970	RQ	40.40 ± 0.03	43.86 ± 0.08	8.67 ± 0.13	-1.63	SFG	-0.16
COSMOS	10012366	150.607120	-1.935110	0.680	RQ	40.15 ± 0.02	43.20 ± 0.20	8.66 ± 0.13	-2.28	SFG	-0.62
COSMOS	10014345	150.713940	-1.972160	1.697	RQ	40.40 ± 0.03	43.78 ± 0.20	8.97 ± 0.14	-2.00	SFG	-0.19
COSMOS	10014743	150.574940	-1.976770	0.863	RL	42.21 ± 0.02	44.33 ± 0.20	7.52 ± 0.11	-0.00	SFG	-0.04
COSMOS	10017028	150.060330	-1.632690	0.554	RQ	39.60 ± 0.03	43.94 ± 0.20	8.73 ± 0.13	-1.60	SFG	-0.50
COSMOS	10018189	150.012040	-1.652110	1.520	RL	41.28 ± 0.03	43.52 ± 0.20	8.16 ± 0.11	-1.45	SFG	1.25
COSMOS	10019570	150.100360	-1.668190	0.620	RL	40.35 ± 0.02	42.67 ± 0.20	8.90 ± 0.14	-3.04	QG	-1.44
COSMOS	10020296	150.206940	-1.680260	1.261	RQ	40.50 ± 0.03	45.20 ± 0.06	8.71 ± 0.13	-0.33	SFG	0.27
COSMOS	10023996	150.312400	-1.730080	0.580	RQ	39.56 ± 0.03	43.89 ± 0.10	8.14 ± 0.11	-1.07	SFG	-0.23
COSMOS	10026655	150.180020	-1.768870	0.350	RL	40.74 ± 0.06	42.41 ± 0.07	9.46 ± 0.18	-3.86	QG	-2.46
COSMOS	10027526	150.244130	-1.782190	1.120	RQ	40.62 ± 0.02	43.38 ± 0.06	8.26 ± 0.11	-1.70	SFG	-0.38
COSMOS	10027888	150.128040	-1.786460	1.574	RQ	40.39 ± 0.03	43.78 ± 0.05	8.87 ± 0.14	-1.90	SFG	-0.17
COSMOS	10038584	150.273380	-1.934240	0.916	RQ	39.89 ± 0.04	44.24 ± 0.02	9.03 ± 0.15	-1.61	SFG	-0.55
COSMOS	10041613	149.842200	-1.605160	1.285	RQ	40.53 ± 0.03	44.48 ± 0.20	8.51 ± 0.12	-0.85	SFG	0.05
COSMOS	10043686	149.559400	-1.631030	0.901	RL	41.38 ± 0.02	42.95 ± 0.20	8.91 ± 0.14	-2.78	SFG	-1.14
COSMOS	10053489	149.592450	-1.756740	1.970	RQ	40.85 ± 0.02	45.08 ± 0.20	9.18 ± 0.16	-0.91	SFG	-1.10
COSMOS	10053620	149.820140	-1.761580	1.440	RQ	40.19 ± 0.03	44.49 ± 0.07	8.01 ± 0.11	-0.33	QG	0.46
COSMOS	10058534	149.564620	-1.823090	1.510	RQ	40.99 ± 0.02	45.18 ± 0.20	7.90 ± 0.11	0.46	SFG	0.20
COSMOS	10061653	149.517180	-1.863480	1.543	RQ	39.78 ± 0.07	44.28 ± 0.08	8.22 ± 0.11	-0.76	SFG	-0.12
COSMOS	10067794	149.781140	-1.932180	1.778	RL	41.89 ± 0.02	43.81 ± 0.13	8.83 ± 0.14	-1.84	QG	-0.51
COSMOS	10074857	150.510680	-2.029220	0.900	RQ	40.25 ± 0.03	43.79 ± 0.04	8.57 ± 0.12	-1.60	SFG	0.06
COSMOS	10076774	150.663700	-2.060240	2.120	RQ	41.24 ± 0.02	44.52 ± 0.20	9.58 ± 0.19	-1.87	SFG	-0.76
COSMOS	10076991	150.447340	-2.053940	0.333	RL	40.71 ± 0.02	41.88 ± 0.12	9.70 ± 0.20	-4.63	QG	-3.50
COSMOS	10084257	150.743420	-2.170530	1.341	RQ	41.40 ± 0.02	44.59 ± 0.20	9.03 ± 0.15	-1.26	SFG	0.16
COSMOS	10084485	150.591320	-2.176420	1.263	RQ	39.95 ± 0.05	43.53 ± 0.20	8.32 ± 0.11	-1.60	SFG	0.21
COSMOS	10084513	150.422270	-2.175360	0.698	RQ	39.38 ± 0.04	44.15 ± 0.02	7.08 ± 0.13	0.26	SFG	0.57
COSMOS	10086247	150.472750	-2.197960	0.404	RL	40.72 ± 0.02	42.65 ± 0.03	8.51 ± 0.12	-2.68	QG	-1.59
COSMOS	10089638	150.630870	-2.255500	1.430	RQ	39.92 ± 0.05	44.24 ± 0.20	8.06 ± 0.11	-0.64	SFG	0.15
COSMOS	10093737	150.378070	-2.318190	1.440	RQ	41.02 ± 0.02	44.42 ± 0.08	8.30 ± 0.11	-0.70	SFG	0.65
COSMOS	10094020	150.442750	-2.322680	1.371	RQ	39.78 ± 0.06	43.57 ± 0.06	8.28 ± 0.11	-1.52	SFG	-0.00
COSMOS	10094905	150.595980	-2.336060	1.090	RQ	40.11 ± 0.03	43.87 ± 0.06	8.29 ± 0.11	-1.23	SFG	0.15
COSMOS	10096301	150.604930	-2.358700	2.694	RQ	40.96 ± 0.03	44.14 ± 0.13	8.14 ± 0.11	-0.82	SFG	0.88
COSMOS	10098600	150.403020	-2.389870	1.267	RQ	40.57 ± 0.03	43.87 ± 0.03	8.58 ± 0.12	-1.53	SFG	-0.21
COSMOS	10100910	150.415700	-2.430200	0.124	RL	38.80 ± 0.02	41.01 ± 0.08	9.17 ± 0.16	-4.97	QG	-2.88
COSMOS	10102594	150.401980	-2.445030	0.120	RQ	37.96 ± 0.03	40.92 ± 0.22	8.74 ± 0.13	-4.64	QG	-2.89
COSMOS	10105342	150.106220	-2.014390	1.954	RL	41.54 ± 0.03	43.93 ± 0.10	9.59 ± 0.19	-2.47	SFG	0.24
COSMOS	10106008	150.343410	-2.019990	0.420	RL	41.22 ± 0.02	42.50 ± 0.06	8.77 ± 0.13	-3.08	QG	-1.72
COSMOS	10108227	150.266430	-2.049850	0.960	RQ	39.96 ± 0.04	43.31 ± 0.13	9.19 ± 0.16	-2.70	SFG	-0.45

Table A1: Radio AGN sample used in the analysis for the fundamental plane (continued).

Survey	ID	R.A.	Decl.	z	Type	$\log\left(\frac{L_R}{\text{erg s}^{-1}}\right)$	$\log\left(\frac{L_X}{\text{erg s}^{-1}}\right)$	$\log\left(\frac{M_{\text{BH}}}{M_\odot}\right)$	$\log \lambda_{\text{Edd}}$	Host galaxy	$\log\left(\frac{\text{sSFR}}{\text{Gyr}}\right)$
(1)	(2)	(3)	(4)	(5)	(6)	(7)	(8)	(9)	(10)	(11)	(12)
COSMOS	10109081	150.042600	2.063280	1.465	RQ	40.13 ± 0.04	44.66 ± 0.02	7.93 ± 0.11	-0.08	SFG	0.41
COSMOS	10110759	150.208000	2.083340	0.758	RQ	39.96 ± 0.02	44.77 ± 0.01	8.18 ± 0.11	-0.23	SFG	-0.66
COSMOS	10111389	150.326900	2.094150	2.164	RQ	41.49 ± 0.02	44.65 ± 0.03	8.46 ± 0.12	-0.63	SFG	0.03
COSMOS	10113383	149.930920	2.118720	2.709	RQ	40.92 ± 0.03	44.47 ± 0.04	8.75 ± 0.13	-1.10	SFG	0.63
COSMOS	10113857	150.115700	2.126740	2.166	RQ	40.12 ± 0.07	44.08 ± 0.11	7.61 ± 0.11	-0.35	SFG	0.79
COSMOS	10120941	150.298770	2.214050	1.150	RQ	39.96 ± 0.04	43.63 ± 0.06	8.53 ± 0.12	-1.71	SFG	-0.04
COSMOS	10121043	149.953480	2.212480	0.474	RL	39.91 ± 0.02	42.35 ± 0.09	8.59 ± 0.12	-3.06	QG	-1.09
COSMOS	10121546	150.059140	2.219940	1.125	RQ	40.88 ± 0.02	43.61 ± 0.05	8.77 ± 0.13	-1.97	SFG	-0.22
COSMOS	10124490	150.002580	2.258650	1.555	RL	42.40 ± 0.02	44.48 ± 0.04	8.61 ± 0.13	-0.94	SFG	0.17
COSMOS	10125460	150.224060	2.270800	1.702	RQ	40.60 ± 0.03	44.55 ± 0.06	8.63 ± 0.13	-0.90	SFG	0.44
COSMOS	10125474	149.940340	2.269370	2.441	RQ	40.95 ± 0.03	45.01 ± 0.07	9.15 ± 0.16	-0.96	SFG	0.47
COSMOS	10130265	149.919800	2.327420	1.131	RQ	40.48 ± 0.03	44.82 ± 0.01	7.89 ± 0.11	0.12	SFG	0.69
COSMOS	10131028	150.171140	2.337050	1.260	RQ	39.59 ± 0.07	44.10 ± 0.08	8.05 ± 0.11	-0.76	SFG	-0.02
COSMOS	10131985	150.073650	2.346850	0.833	RQ	39.68 ± 0.03	44.24 ± 0.03	6.89 ± 0.14	0.53	SFG	0.62
COSMOS	10134934	150.288540	2.381910	1.581	RQ	40.96 ± 0.03	43.72 ± 0.08	9.09 ± 0.15	-2.18	SFG	0.50
COSMOS	10135522	150.058090	2.380430	0.350	RL	39.63 ± 0.02	41.73 ± 0.08	8.90 ± 0.14	-3.98	QG	-2.44
COSMOS	10136176	149.905940	2.396450	0.742	RL	41.01 ± 0.02	42.89 ± 0.08	8.40 ± 0.12	-2.31	SFG	-0.58
COSMOS	10136788	150.174000	2.402980	0.979	RQ	39.37 ± 0.07	44.08 ± 0.02	7.11 ± 0.13	0.16	SFG	0.55
COSMOS	10138319	150.181440	2.423420	0.727	RL	40.28 ± 0.02	42.97 ± 0.08	8.74 ± 0.13	-2.58	QG	-1.17
COSMOS	10144600	149.547800	2.033080	1.579	RL	41.10 ± 0.02	43.36 ± 0.19	8.01 ± 0.11	-1.47	SFG	0.44
COSMOS	10144923	149.419950	2.035540	0.734	RQ	39.74 ± 0.04	44.66 ± 0.20	6.83 ± 0.14	1.02	SFG	1.03
COSMOS	10145065	149.396200	2.034520	0.294	RQ	39.47 ± 0.03	42.57 ± 0.20	7.56 ± 0.11	-1.80	SFG	-0.07
COSMOS	10148505	149.673140	2.078660	1.773	RQ	40.50 ± 0.04	45.13 ± 0.16	9.01 ± 0.15	-0.69	SFG	0.14
COSMOS	10148583	149.497970	2.076670	1.757	RQ	40.03 ± 0.07	44.58 ± 0.20	8.25 ± 0.11	-0.48	SFG	0.01
COSMOS	10155880	149.827970	2.164330	0.889	RQ	40.98 ± 0.02	45.07 ± 0.01	7.62 ± 0.11	0.63	SFG	-0.13
COSMOS	10157147	149.885450	2.177170	0.660	RQ	40.16 ± 0.03	43.52 ± 0.04	8.83 ± 0.14	-2.13	SFG	-0.39
COSMOS	10159865	149.649640	2.209250	0.953	RL	41.24 ± 0.02	42.96 ± 0.14	9.03 ± 0.15	-2.89	QG	-1.17
COSMOS	10161631	149.648830	2.232750	0.670	RQ	40.16 ± 0.02	43.10 ± 0.11	9.03 ± 0.15	-2.74	SFG	-1.16
COSMOS	10163898	149.743930	2.249740	0.130	RQ	39.11 ± 0.02	42.78 ± 0.01	8.42 ± 0.12	-2.46	SFG	-1.61
COSMOS	10164140	149.572400	2.262690	0.706	RQ	41.07 ± 0.02	44.33 ± 0.20	8.70 ± 0.13	-1.18	SFG	-0.54
COSMOS	10164461	149.693280	2.267480	0.905	RL	41.52 ± 0.02	43.31 ± 0.11	8.01 ± 0.11	-1.52	QG	-0.21
COSMOS	10165881	149.891970	2.285120	2.937	RQ	40.99 ± 0.03	45.17 ± 0.02	9.49 ± 0.18	-1.13	SFG	-0.01
COSMOS	10166552	149.441480	2.287580	0.480	RL	40.84 ± 0.02	43.37 ± 0.20	8.67 ± 0.13	-2.12	QG	-0.97
COSMOS	10169163	149.761540	2.318430	0.350	RQ	38.88 ± 0.03	44.11 ± 0.01	7.49 ± 0.11	-0.19	SFG	-0.46
COSMOS	10169901	149.793800	2.327210	0.890	RQ	39.56 ± 0.04	43.58 ± 0.06	8.78 ± 0.13	-2.02	SFG	-0.64
COSMOS	10176857	149.839020	2.407780	0.730	RQ	39.95 ± 0.02	42.77 ± 0.09	9.33 ± 0.17	-3.37	QG	-1.27
COSMOS	10179656	149.597140	2.441240	1.170	RQ	40.14 ± 0.02	43.40 ± 0.20	7.82 ± 0.11	-1.23	SFG	0.54
COSMOS	10181467	150.639040	2.464400	0.800	RQ	39.79 ± 0.03	44.14 ± 0.03	8.71 ± 0.13	-1.39	SFG	-0.30
COSMOS	10183814	150.379800	2.490180	0.350	RL	40.61 ± 0.02	42.35 ± 0.04	8.98 ± 0.15	-3.45	QG	-2.13
COSMOS	10189778	150.683180	2.574640	0.573	RQ	39.19 ± 0.04	43.54 ± 0.20	8.79 ± 0.13	-2.07	SFG	-0.99
COSMOS	10192709	150.521000	2.625440	0.520	RQ	40.29 ± 0.02	44.12 ± 0.20	9.21 ± 0.16	-1.90	SFG	-1.70
COSMOS	10192764	150.705570	2.629600	1.767	RL	42.53 ± 0.02	44.69 ± 0.20	8.32 ± 0.11	-0.44	SFG	0.25
COSMOS	10195541	150.620060	2.671380	3.140	RQ	41.27 ± 0.03	45.05 ± 0.20	9.46 ± 0.18	-1.22	SFG	0.01
COSMOS	10195703	150.683720	2.672750	0.670	RQ	40.37 ± 0.02	44.20 ± 0.20	8.40 ± 0.12	-1.01	SFG	-1.02
COSMOS	10199183	150.426010	2.725190	1.661	RQ	41.08 ± 0.03	43.88 ± 0.20	9.62 ± 0.19	-2.55	SFG	-0.27
COSMOS	10200729	150.446880	2.749520	1.165	RQ	40.28 ± 0.03	44.24 ± 0.20	9.07 ± 0.15	-1.65	QG	-0.33
COSMOS	10201379	150.435960	2.758880	1.140	RQ	39.90 ± 0.04	45.25 ± 0.20	8.17 ± 0.11	0.27	SFG	0.05
COSMOS	10206501	150.130360	2.472150	0.926	RQ	39.62 ± 0.04	43.55 ± 0.05	8.74 ± 0.13	-2.01	QG	-0.84
COSMOS	10208978	149.977890	2.504240	1.171	RL	41.42 ± 0.02	43.75 ± 0.10	8.53 ± 0.12	-1.59	QG	-0.19
COSMOS	10210031	150.022420	2.516580	0.680	RQ	40.07 ± 0.02	43.50 ± 0.03	8.75 ± 0.13	-2.07	QG	-0.73
COSMOS	10210442	150.132320	2.523310	1.319	RQ	39.70 ± 0.06	44.08 ± 0.07	8.04 ± 0.11	-0.77	SFG	0.20
COSMOS	10210564	149.915730	2.521330	0.728	RL	40.12 ± 0.02	42.80 ± 0.08	9.03 ± 0.15	-3.05	QG	-1.04
COSMOS	10214987	150.333630	2.578830	3.751	RL	43.43 ± 0.02	43.81 ± 0.20	8.83 ± 0.14	-1.83	SFG	0.74
COSMOS	10215907	149.938320	2.577570	0.120	RQ	38.81 ± 0.02	42.00 ± 0.09	8.50 ± 0.12	-3.31	QG	-1.84
COSMOS	10220261	150.335130	2.642880	2.899	RQ	41.06 ± 0.03	44.48 ± 0.20	8.00 ± 0.11	-0.33	SFG	1.12
COSMOS	10221707	149.955170	2.657900	2.205	RQ	40.29 ± 0.05	43.81 ± 0.14	9.10 ± 0.15	-2.10	SFG	-0.24
COSMOS	10225941	150.042330	2.694830	0.248	RL	40.18 ± 0.02	42.14 ± 0.11	8.74 ± 0.13	-3.42	QG	-2.22
COSMOS	10226706	150.110410	2.708290	0.350	RL	40.49 ± 0.02	41.88 ± 0.20	9.07 ± 0.15	-4.01	QG	-2.11
COSMOS	10230501	149.998500	2.769160	0.170	RL	39.94 ± 0.02	41.41 ± 0.20	9.15 ± 0.16	-4.56	QG	-2.35
COSMOS	10231301	150.230470	2.778020	1.944	RQ	40.00 ± 0.07	44.17 ± 0.20	7.77 ± 0.11	-0.41	SFG	0.55
COSMOS	10232138	150.347530	2.788730	1.758	RQ	40.54 ± 0.03	44.83 ± 0.20	8.67 ± 0.13	-0.66	SFG	-0.04
COSMOS	10235445	149.659970	2.465100	1.010	RQ	40.16 ± 0.03	43.78 ± 0.20	9.25 ± 0.16	-2.28	SFG	-1.02
COSMOS	10241023	149.478880	2.521840	0.228	RL	39.44 ± 0.02	41.20 ± 0.20	8.26 ± 0.11	-3.87	SFG	-0.87
COSMOS	10253346	149.472720	2.687290	1.453	RQ	40.84 ± 0.02	44.27 ± 0.20	8.86 ± 0.14	-1.41	SFG	-0.20
COSMOS	10253580	149.734150	2.691090	0.910	RL	41.34 ± 0.02	43.00 ± 0.20	7.84 ± 0.11	-1.65	SFG	1.02
COSMOS	10257260	149.838840	2.736780	0.220	RQ	39.72 ± 0.02	43.80 ± 0.06	6.28 ± 0.18	0.71	SFG	0.21
COSMOS	10257734	149.525570	2.744430	0.899	RQ	39.52 ± 0.05	44.37 ± 0.20	8.46 ± 0.12	-0.90	SFG	-0.38
COSMOS	10260713	149.895980	2.783570	0.664	RQ	39.53 ± 0.03	42.87 ± 0.20	7.93 ± 0.11	-1.88	SFG	-0.30
COSMOS	10005564	150.657710	1.801750	2.464	RQ	41.18 ± 0.03	44.38 ± 0.20	8.95 ± 0.14	-1.39	SFG	0.43
COSMOS	10078654	150.496570	2.089290	1.150	RQ	40.11 ± 0.03	43.86 ± 0.20	8.70 ± 0.13	-1.66	SFG	-0.33
COSMOS	10078991	150.474720	2.094080	1.261	RQ	40.64 ± 0.03	43.94 ± 0.20	8.22 ± 0.11	-1.09	SFG	0.62